

Industry-applicable, efficient hydrogen evolution reaction through an interface-activated bimetallic electrode with seawater photolysis in alkaline media

Ashwani Kumar^{1,2,#}, Viet Q. Bui^{1,2,#}, Jinsun Lee^{1,2}, Amol R. Jadhav¹, Yoseph Whang^{1,2}, Min Gyu Kim³, Yoshiyuki Kawazoe⁴, and Hyoyoung Lee^{* 1,2}

¹Center for Integrated Nanostructure Physics (CINAP), Institute for Basic Science (IBS), Sungkyunkwan University, Suwon 16419, Korea

²Department of Chemistry, Sungkyunkwan University (SKKU), Suwon, 16419, Republic of Korea

³Beamline Research Division, Pohang Accelerator Laboratory (PAL), Pohang University of Science and Technology, Pohang 37673, Republic of Korea

⁴New Industry Creation Hatchery Center, Tohoku University, Sendai, 980-8579, Japan

*Email of correspondence: hyoyoung@skku.edu

Equal contribution

Hydrogen evolution reaction (HER) electrocatalysts over platinum (Pt) in an alkaline medium is crucial for hydrogen economy. Herein, we demonstrate new concept “interface-active electrode” to transform naturally inert alkaline HER materials towards industry-applicable HER electrocatalyst, comprised of interface-rich NiP₂-FeP₂ on Cu nanowires that required overpotential as low as 23.6 and 357 mV at -10 and -1000 mA/cm², respectively, with exceptional stability at the industrial current density of -1 A cm⁻², superior to commercial Pt under alkaline solution. Structural characterization and theoretical calculations revealed the abundant interface between facets of NiP₂-FeP₂ on Cu exhibits optimum H adsorption-free energy than Pt and lower kinetic barrier for water dissociation ($\Delta G_B = 0.16$ eV), boosting alkaline HER. Additionally, when integrated in a water splitting device, generated 10 mA/cm² at only 1.42, 1.4, and 1.31 V under 1 M KOH, artificial seawater

at 25 °C and 100 °C, respectively, along with high solar-to-hydrogen (STH) conversion efficiency of 19.85 %.

Hydrogen fuel production from electrochemical water splitting is a promising route for a clean energy source and a potential alternative to the use of traditional fossil fuels.¹⁻³ With the limited supply of fresh water on our planet, earth-abundant seawater electrolysis via direct solar energy is a highly appealing means for energy conversion and storage technology.^{4,5} Electrochemical water splitting for H₂ production can be accomplished in acidic and alkaline media at the industrial scale. However, this demands a significantly high cell voltage of around 1.8-2.4 V, which is higher than the thermodynamic value of 1.23 V.⁶ Although there have been numerous efforts to develop an acidic water electrolyzer, the high cost of the proton exchange membrane with sluggish oxygen evolution kinetics hampers its commercial application.⁷ A suitable alternative is low-cost alkaline electrolyzers, which are compatible with non-noble metals but suffer from sluggish kinetics of the HER in alkaline media, requiring an additional water dissociation step which is unseen in acidic HER.⁸ Currently, noble metal platinum (Pt) is the benchmarking catalyst for the HER in acidic media. However, its high cost (the US \$29,066 per kg) and two-three orders of magnitude lower activity in alkaline media hinder its commercial application in alkaline electrolyzers.^{9,10} Therefore, it is of both fundamental and technological significance to develop low-cost non-noble metal-based HER electrocatalysts with superior performance over Pt in alkaline media for large-scale hydrogen production (e.g., transition metal oxides¹¹, sulfides¹², phosphides¹³, selenides¹⁴, carbides¹⁵, nitrides¹⁶, or alloys¹⁷).

Among them, transition metal-based phosphides have received immense attention due to their promising HER performance owing to their distinctive charge nature (M⁺ and P⁻) with modulation of the electronic parameters as well as hydrogen adsorption behavior.^{18,19} More interestingly, the

fabrication of heterojunctions in multi-metal-based phosphides can create more suitable interfaces for activating the reaction intermediates along with the advantage of synergistic metal-metal interactions.^{20,21} However, the precise roles as well as the real active sites for water dissociation and hydrogen adsorption have rarely been investigated and remain speculative.²² In addition, the overall electronic conductivity, rarely available active sites, suppressed mass diffusion, and insufficient intrinsic activity hampers their performance, which needs to be optimized to achieve the crucial Pt-like HER activity and stability for large scale hydrogen production.^{23,24} The current need is to develop a self-supported 3D core-shell nanostructured electrode with a large surface area and exposed active sites firmly anchored on a conductive substrate, which can significantly overcome the contact issue of the catalyst and skips the use of an additional conductive polymer binder. Moreover, it can also avoid the need for additional current collectors such as a glassy carbon electrode (GCE) or another collector (Ni/Cu/Co foams and foils), hence significantly reducing the fabrication cost.^{18,25,26} Recently, Yu *et al.* reported a core-shell catalyst (Cu nanowire shelled with NiFe-LDH) for overall water splitting where metallic Cu serves as the conducting core for overcoming the poor electrical conductivity of the shell. However, the role of Cu towards the enhancement of the intrinsic activity of the hybrid was not elucidated, and the origin of the high performance remains unclear.^{27,28} Nevertheless, the excellent electrical conductivity of Cu makes it a perfect choice as a substrate material, whereas Cu_{NW} directly grown on the Cu substrate in a cheaper and easier way can serve as a highly conducting core material, ensuring excellent electrical conductivity. Therefore, developing a self-supported electrocatalyst with a conducting core and exposed active shell based on earth-abundant metals with exceptional activity even better than commercial Pt for HER is of prime importance for high-purity hydrogen production on the industrial scale.

Herein, we report a novel strategy for an industry-applicable, highly active self-supported core-shell HER electrocatalyst superior to Pt in alkaline media, which is high performing for complete water splitting. Using a facile and simple process, we fabricated highly active interface-rich NiP₂-FeP₂ anchored on a metallic Cu_{NW} core self-supported on commercial Cu foam (NiP₂-FeP₂/Cu_{NW}/Cu_f), ensuring strong mechanical integrity of the hybrid with the Cu current collector. The integrated hybrid electrode exhibited exceptional HER activity in alkaline media with very low overpotential values of 23.6, 323, and 357 mV to achieve -10, -500, and -1000 mA cm⁻², respectively, excellent stability, and nearly 100% faradaic efficiency, which is superior to commercial Pt. Density functional theory (DFT) calculations reveal that the incorporation of Cu_{NW} support to the interface-rich NiP₂-FeP₂ not only efficiently optimizes the ΔG_{H^*} of the hybrid nanostructure but also remarkably reduces the kinetic barrier for water dissociation in alkaline media, thereby resulting in exceptional HER performance. In addition, the complete electrolyzer, NiP₂-FeP₂/Cu_{NW}/Cu_f (-) || NiFe-LDH/Ni_f (+) (LDH = layered double hydroxide), achieves 10 mA/cm² at only 1.42, 1.4, and 1.31 V under 1 M KOH and 1 M KOH with 0.6 M NaCl (artificial seawater-25 °C) and artificial seawater-100 °C, respectively, along with superior stability. When integrated with a commercial Si solar cell, the integrated system yields stable seawater splitting photocurrent with an STH conversion efficiency of 19.85% under artificial seawater-100 °C, demonstrating its potential for practical applications.

Results

Electrocatalyst preparation and structural characterization. The synthetic process for the fabrication of the NiP₂-FeP₂/Cu_{NW}/Cu_f hybrid architecture is schematically illustrated in Fig. 1. Briefly, the surface of thoroughly cleaned Cu foam was chemically oxidized to grow Cu(OH)₂ nanowires on the Cu foam (Cu(OH)₂_{NW}/Cu_f) followed by calcination in air at 180 °C to yield CuO

nanowires ($\text{CuO}_{\text{NW}}/\text{Cu}_f$). Then, the CuO_{NW} was electrochemically reduced to metallic Cu_{NW} on Cu foam ($\text{Cu}_{\text{NW}}/\text{Cu}_f$), which is a safe and low-cost approach compared to annealing under a hydrogen atmosphere. The transformation of the Cu foam to $\text{Cu}_{\text{NW}}/\text{Cu}_f$ was tracked by X-ray diffraction (XRD) (Fig. 2a) and field emission scanning electron microscope (FESEM) images (Supplementary Figs. 1a, b, and c). Fig. 2a confirms the successful synthesis of $\text{Cu}(\text{OH})_2$ (JCPDS 080-0656), CuO (JCPDS 080-1916), and the highly conducting face-centered cubic (FCC) metallic Cu_{NW} (JCPDS 04-0836) on the Cu foam.^{29,30} Supplementary Figs. 1a and b show low and high magnification images of 1D $\text{Cu}(\text{OH})_2$ NW grown on the surface of the 3D porous Cu foam, respectively, whereas Supplementary Fig. 1c reveals uniformly grown 1D metallic Cu_{NW} with an average diameter of 110 ± 10 nm. After the successful synthesis of the Cu_{NW} core, a 2D NiFe-LDH shell was uniformly and vertically electrodeposited on the surface of the Cu_{NW} core on the Cu foam ($\text{NiFe-LDH}/\text{Cu}_{\text{NW}}/\text{Cu}_f$) with an average size of the core-shell heterostructure of 152 ± 8 nm, as revealed in the FESEM image in Supplementary Fig. 1d. The energy dispersive X-ray analysis (EDS) pattern confirms the presence of Ni, Fe, O, and Cu with a Ni to Fe ratio of 0.954, corroborating the successful deposition of NiFe-LDH on the Cu_{NW} core (Supplementary Fig. 2a). Finally, the resulting NiFe-LDH on Cu_{NW} was thermally phosphorized to obtain the $\text{NiP}_2\text{-FeP}_2$ shell on Cu_{NW} ($\text{NiP}_2\text{-FeP}_2/\text{Cu}_{\text{NW}}/\text{Cu}_f$) via a vapor phase phosphidation process using sodium hypophosphite as the phosphorus source under an argon atmosphere. After the phosphidation of LDH to yield $\text{NiP}_2\text{-FeP}_2$ on the Cu_{NW} core-shell heterostructure, the average size decreased from 152 ± 8 nm to 122 ± 8 nm (Supplementary Fig. 1e), suggesting an average shell thickness of 10-12 nm firmly anchored on the metallic Cu_{NW} core. The XRD pattern (Fig. 2b) reveals the formation of $\text{NiP}_2\text{-FeP}_2$ on the metallic Cu_{NW} with strong diffraction peaks originating from the cubic NiP_2 (JCPDS 21-0590)³¹ and FeP_2 (JCPDS 89-2261)³² along with diffraction of the metallic Cu core.

The EDS pattern confirms the existence of Ni, Fe, P, and Cu with a Ni:Fe:P ratio of 1.17:1:1.96, which is consistent with the phases of the Ni and Fe phosphides deduced from the XRD pattern, whereas, for only NiP₂/Cu_{NW}/Cu_f and FeP₂/Cu_{NW}/Cu_f electrode, the ratio between Ni:P and Fe:P, respectively, are also almost 1:2, similar with the metal to phosphorus ratio of the main electrode (Supplementary Figs. 2b, c, d). The NiP₂-FeP₂ grown on carbon fiber paper (NiP₂-FeP₂/CFP) was also characterized by XRD, FESEM, and EDS (Supplementary Fig. 3). The transmission electron microscopy (TEM) image in Fig. 2c further confirms the core-shell nanostructure with strong anchoring of the NiP₂-FeP₂ shell on the Cu_{NW} core, forming a porous surface morphology with exposed active sites with copious channels for smooth electrolyte diffusion and gaseous product release, whereas the conducting metallic Cu core is expected to enhance the electron transfer rate during the reaction. The high-resolution transmission electron microscopy (HRTEM) image in Fig. 2d and Supplementary Fig. 4a clearly reveals the formation of an interface between the NiP₂ and FeP₂ based on well-resolved lattice spacings of 0.32 and 0.21 nm corresponding to the (111) plane of NiP₂ and the (111) plane of FeP₂, respectively, which is firmly anchored on the metallic Cu core with a lattice spacing of 0.2 nm corresponding to the (111) reflection of the metallic Cu. The corresponding selected area electron diffraction (SAED) pattern also shows the presence of diffraction rings corresponding to these lattice planes (Fig. 2d inset). HRTEM image in Supplementary Fig. 4b taken at the different locations also reveals the formation of an interface between (210) and (101) plane of NiP₂ and FeP₂, respectively. To determine the distribution of Ni, Fe, Cu, and P elements, scanning transmission electron microscopy (STEM) high-angle annular dark-field (HAADF) elemental mapping were carried out, confirming the uniform distribution of Ni, Fe, Cu, and P in the NiP₂-FeP₂/Cu_{NW} heterostructure (Fig. 2e).

The elemental composition and valence states of the elements on the surface of the NiP₂-

FeP₂/Cu_{NW}/Cu_f electrode were further studied by X-ray photoelectron spectroscopy (XPS) (Fig. 3). According to the high-resolution core-level XPS spectra, we can detect the presence of Ni, Fe, Cu, and P on the surface of the NiP₂-FeP₂/Cu_{NW}/Cu_f electrode (Figs. 3a, b, c, and d). The Cu 2p spectra in Fig. 3a reveals the presence of metallic Cu at a binding energy of 932.6 and 952.5 eV along with the surface oxidized Cu²⁺ species at a binding energy of 934.8 and 954.7 eV.³³ The broad peak at a binding energy of 943.1 eV is attributed to the satellite of the Cu 2p_{3/2} peak. The small peak at a binding energy of 932.8 eV³⁴ corresponds to Cu^{δ+} in the Cu 2p_{3/2} spectra, which may have arisen due to the bonding between Cu and P from the metal phosphide, affirming the strong anchoring of the metal phosphide on the metallic Cu core. However, after argon ion sputtering, only metallic Cu, along with small Cu^{δ+} peaks, are dominant without any surface oxides, suggesting the presence of highly conducting metallic Cu core. The Ni 2p spectrum in Fig. 3b shows three different peaks after deconvolution with binding energies of 853.3, 856.1, and 859.6 eV corresponding to Ni^{δ+} (0 < δ < 2) originating from the NiP₂, Ni²⁺ (oxidized Ni species), and the satellite peak of Ni 2p_{3/2}, respectively, whereas, peak at 874.4 and 879 eV corresponds to Ni²⁺ (oxidized Ni species), and the satellite peak of Ni 2p_{1/2}, respectively.³¹ After argon etching, the dominant peaks at 853.2 and 870.2 eV corresponds to Ni-P bonding are in consistent with the XRD pattern. Similarly, in the high-resolution XPS spectra of Fe 2p (Fig. 3c), the peak centered at a binding energy of 707.7 eV can be ascribed to Fe^{δ+} (0 < δ < 3), which mainly originates from the Fe-P bonding in FeP₂, whereas the peaks at binding energies of 710.3, 712.2, and 714.2 eV can be ascribed to the surface oxidized Fe²⁺, Fe³⁺, and a satellite peak of Fe 2p_{3/2}, respectively, whereas, peak at 723.5, 725.2 and 726.6 eV corresponds Fe²⁺, Fe³⁺, and a satellite peak of Fe 2p_{1/2}, respectively.³⁵ After argon sputtering, the dominant peaks at 707.7 and 720.3 eV corresponds to the Fe-P bonding in FeP₂, which is also consistent with the XRD pattern. Both the high-resolution

XPS spectra of Ni 2p and Fe 2p confirm the bonding between the metal and phosphide with metals bearing a partial positive charge due to the strong electron-withdrawing effect from P. As revealed in the P 2p XPS spectra (Fig. 3d), the peak located at 129.1 eV is ascribed to reduced phosphorous in the form of Ni and Fe phosphide, whereas the peak at 133.6 eV corresponds to the surface oxidized phosphorous in phosphate (P^{3+} or P^{5+}), which is commonly seen in metal phosphides exposed to air, whereas, after argon sputtering the peak corresponding to Ni and Fe phosphide are highly dominant compared with the oxidized states of phosphorus, suggesting the successful synthesis of metal phosphide. The binding energy of 129.1 eV is faintly lower than that of elemental P (130 eV), indicating a partial negative charge possessed by P ($P^{\delta-}$), which can significantly trap protons during catalysis and enhance the performance.¹⁸ More importantly, Supplementary Fig. 5 reveals that there is an electron transfer between the NiP_2 and FeP_2 components benefitting from the effective contact between them at the interface in the heterostructure, which is crucial for regulating the catalytic activity. The above XPS analysis result demonstrates the successful synthesis of well-anchored NiP_2 - FeP_2 on the metallic Cu core.

To further explore the chemical and structural information on the NiP_2 - FeP_2 / Cu_{NW} / Cu_f electrode, X-ray absorption near-edge structure (XANES), and the corresponding Fourier transform of extended X-ray absorption fine structure (EXAFS) spectroscopy were precisely investigated (Fig. 4). The Cu K-edge XANES spectra of the NiP_2 - FeP_2 / Cu_{NW} / Cu_f electrode, along with other control samples, coincides with that of the Cu foil, suggesting the metallic state of the Cu and matches with the XRD and XPS results (Fig. 4a). In the Ni K-edge XANES spectra, the valence of NiP_2 - FeP_2 / Cu_{NW} / Cu_f and NiP_2 / Cu_{NW} / Cu_f electrode were lower than that of NiO, suggesting deep phosphidation feature (Fig. 4b). Analogously, the Fe K-edge XANES spectra of NiP_2 - FeP_2 / Cu_{NW} / Cu_f and FeP_2 / Cu_{NW} / Cu_f electrode also shows a lower valence than that of Fe_2O_3 ,

illustrating the successful phosphidation treatment (Fig. 4c). Both the Ni K-edge and Fe K-edge XANES spectra agree with the XRD and XPS results. The Fourier transformed (FT) Cu K-edge EXAFS spectra of the NiP₂-FeP₂/Cu_{NW}/Cu_f electrode reveals the presence of the dominant Cu-Cu peak at 2.25 Å along with partially formed Cu-P bonding at 1.82 Å, consistent with the XPS result (Fig. 4d).³⁶ In the FT Ni K-edge EXAFS spectra of the NiP₂-FeP₂/Cu_{NW}/Cu_f electrode, the bands centered at 1.91 Å and 2.36 Å corresponds to Ni-P and Ni-Ni (P-bridged), respectively, whereas the bands centered at 2.04 Å and 2.61 Å in the FT Fe K-edge EXAFS spectra corresponds to Fe-P and Fe-Fe (P-bridged), respectively, confirming the successful phosphidation treatment to yield NiP₂-FeP₂ (Fig. 4e, f).^{37,38} However, the signature of surface oxidation displayed in the XPS data of the pristine NiP₂-FeP₂/Cu_{NW}/Cu_f electrode can also be confirmed from the appearance of the Ni-O and Fe-O bonds in the EXAFS spectra of Ni K-edge and Fe K-edge, respectively. These XANES and EXAFS results combined with XRD and XPS investigations, demonstrate the successful synthesis of abundant interface rich NiP₂-FeP₂ anchored on metallic Cu core. As a consequence of the successful synthesis of the interface-rich NiP₂-FeP₂ on metallic Cu, the highly porous nature with exposed active sites along with the conducting Cu core is likely to synergistically function together to achieve exceptionally high electrocatalytic performance.

Electrochemical alkaline hydrogen evolution catalysis. The electrocatalytic HER performance was evaluated in a typical three-electrode system under alkaline media (1 M KOH) with the designed electrodes as the working electrode, Ag/AgCl as the reference electrode, and platinum mesh as the counter electrode. All of the potentials were iR-corrected and converted to the reversible hydrogen electrode (RHE) scale.³⁹ As revealed in the linear sweep voltammetry (LSV) polarization curve in Figs. 5a and b, the NiP₂-FeP₂/Cu_{NW}/Cu_f hybrid electrode exhibit outstanding HER activity requiring only a 23.6 mV overpotential to attain a current density of -10 mA cm⁻²,

which is almost 14 times lower than that of the NiP₂-FeP₂/CFP ($\eta_{10} = 323$ mV) electrode, emphasizing the efficacious role of the metallic Cu_{NW} core towards superior performance. It is interesting to observe that the HER cathodic current density for the NiP₂-FeP₂/Cu_{NW}/Cu_f electrode increases drastically, reaching current industrial densities of -500 and -1,000 mA cm⁻² at overpotentials of only 323 and 357 mV, respectively, making it suitable for real industrial applications (Fig. 5b). Supplementary Figs. 6a, b, and c show that the optimized electrodeposition time is 60 sec, whereas the Ni to Fe phosphide ratio of 1:1 is the optimized composition for superior HER performance. To confirm that the superior performance is intrinsic to our electrode rather than any possible Pt contamination during the NiFe-LDH electrodeposition, we analyzed the XPS spectra of the NiFe-LDH/Cu_{NW}/Cu_f Electrode which confirm that the Ni and Fe were successfully deposited without any Pt incorporation (Supplementary Fig. 7). Surprisingly, the performance of the NiP₂-FeP₂/Cu_{NW}/Cu_f electrode made solely of earth-abundant elements is even superior to that of the highly celebrated state-of-the-art 20 wt% Pt/C/Cu_f electrode which requires 32, 474, and 756 mV to reach -10, -500, and -1,000 mA cm⁻², respectively, with a similar mass loading (Figs. 5a, b and Supplementary Fig. 8). To gain more insight into the HER kinetics, the Tafel slope was estimated to probe the rate-determining steps during the HER process using the Tafel equation:

$$\eta = b \log(j) + a \quad (1)$$

where η is the overpotential, j is the current density, and b is the Tafel slope. As revealed in Fig. 5c, the Tafel slope for NiP₂-FeP₂/Cu_{NW}/Cu_f is only 52 mV dec⁻¹ in the low overpotential range, which is much lower than those of NiP₂-FeP₂/CFP (155 mV dec⁻¹) and even 20 wt% Pt/C/Cu_f electrodes (65 mV dec⁻¹). This suggests the most favorable HER kinetics follow the Volmer-Heyrovsky mechanism, where the electrochemical desorption step (Heyrovsky step) is the rate-determining step.⁴⁰ Moreover, measurements conducted at a slower scan rate in order to maintain

the steady-state condition revealed that the high intrinsic HER performance with a similar Tafel slope value was well maintained for the NiP₂-FeP₂/Cu_{NW}/Cu_f electrode and is still better than that of the 20 wt% Pt/C/Cu_f electrode (Supplementary Fig. 9). Furthermore, to corroborate the remarkably high HER performance, electrochemical impedance spectroscopy (EIS) and double-layer capacitance (C_{dl}) were investigated. The Nyquist plot in Fig. 5d recorded at a η value of 374 mV reveals that the NiP₂-FeP₂/Cu_{NW}/Cu_f possesses the lowest charge transfer resistance (R_{CT}) of only 0.6 Ω compared to NiP₂-FeP₂/CFP (2.94 Ω) and commercial 20 wt% Pt/C/Cu_f (1.1 Ω), suggesting rapid electron transfer kinetics at the interface between the electrode and electrolyte. This demonstrates the pivotal role of the Cu_{NW} core towards superior intrinsic conductivity of the hybrid structure and the significance of binding between the metal phosphide shell with the Cu core in enhancing the electron transfer rate during the HER. Similarly, the estimated C_{dl} value, which is directly proportional to the electrochemically active surface area (ECSA), for NiP₂-FeP₂/Cu_{NW}/Cu_f is also higher (19.8 mF cm⁻²) compared to NiP₂-FeP₂/CFP (2.26 mF cm⁻²), implying that the hybrid structure significantly enhances the available active sites necessary for attaining the industrial high current density (Fig. 5e and Supplementary Figs. 10a and b). The superior intrinsic performance, as well as the effective role of the Cu_{NW} core, was corroborated by normalizing the catalytic current of NiP₂-FeP₂/Cu_{NW}/Cu_f and NiP₂-FeP₂/CFP by their respective ECSA values (Supplementary Fig. 11). To confirm that the high electrocatalytic HER activity is indeed intrinsic to the NiP₂-FeP₂/Cu_{NW}/Cu_f electrode instead of any possible Pt contamination from the counter electrode, we investigated the HER activity using a graphite rod and Pt mesh as the counter electrode and found that both the LSV polarization curves follow similar traces (Supplementary Fig. S12). The performance of the NiP₂-FeP₂/Cu_{NW}/Cu_f is also comparable to that of 20 wt% Pt/C/Cu_f under different pH range (14-10) in the basic media (Supplementary Fig. 13).

However, due to the decreasing conductivity of the electrolyte with decreasing pH, the performance and the current density in both cases also decreases, solely due to the hindered electron transfer rate owing to the poor electrical conductivity of the electrolyte.

Apart from the superior HER performance of the NiP₂-FeP₂/Cu_{NW}/Cu_f electrode, long-term stability testing at an industrial high current density is one of the crucial parameters for realizing large-scale hydrogen production. The chronopotentiometry test confirmed the superior durability for the NiP₂-FeP₂/Cu_{NW}/Cu_f electrode at an industrial current density of -1 A cm⁻² for 50 h with the continuous smooth release of hydrogen gas bubbles without any bubble accumulation signature, whereas the commercial Pt/C shows relatively poor stability at the same current density, with bubble accumulation signatures (Fig. 5f). The stability test for NiP₂-FeP₂/Cu_{NW}/Cu_f at a smaller η value of only 25 mV also confirmed its superior intrinsic activity and stability (Supplementary Fig. 14). Post stability characterizations after chronopotentiometry test at a high current density of -1 A cm⁻² confirms that the crystal structure, morphology, and composition of our electrode remains unaltered (Supplementary Fig. 15). The XRD pattern and morphology, along with the active interface between NiP₂-FeP₂ as well as the composition between the elements, are well maintained after the long-term stability test (Supplementary Figs. 15a, b, c, d, and e). The high-resolution XPS spectra of Ni 2p_{3/2}, Fe 2p_{3/2}, and P 2p of the electrode after the stability test are almost identical to that of the fresh electrode, also suggesting the superior stability of our electrode. However, there was a slight reduction of the surface copper oxides under the reduction potential revealed in the Cu 2p_{3/2} XPS spectra (Supplementary Figs. 15f, g, h, and i). The potential of the reference electrode remains unaltered after the stability test in alkaline media (Supplementary Fig. 16). Apart from the superior activity and stability, the excellent energy conversion efficiency is also an important benchmark for an efficient electrocatalyst. The NiP₂-

FeP₂/Cu_{NW}/Cu_f electrode exhibited excellent energy conversion efficiency with faradaic efficiencies of 98.2 and 98.5% at current densities of -200 and -500 mA cm⁻², respectively, which were measured by collecting the actual amount of hydrogen gas evolved using a water displacement method (Supplementary Fig. 17). This exceptional activity, as well as the stability of the NiP₂-FeP₂/Cu_{NW}/Cu_f electrode under alkaline conditions, is comparable to and even better than most recently reported electrocatalysts (Supplementary Table 1). The HER activity of the NiP₂-FeP₂/Cu_{NW}/Cu_f is highly reproducible as well as consistent (Supplementary Fig. 18). Additionally, to show that our facile method to fabricate highly active interface activated HER electrode can be effectively scaled up to meet the prerequisite for practical applications, we fabricated large sizes of electrodes (2cm*2cm and 5cm*5cm) on Cu foam and test them towards hydrogen generation (Supplementary Fig. 19). The optical images in Supplementary Figs. 19a, b, c, d, and e show the large size of Cu_f, Cu(OH)₂ NW/Cu_f, Cu_{NW}/Cu_f, NiP₂-FeP₂/Cu_{NW}/Cu_f, and NiP₂-FeP₂/Cu_{NW}/Cu_f electrode bend to form a ring, respectively. The LSV polarization curve in Supplementary Fig. 19f shows the enormous amount of current generated from these large-sized electrodes at low voltages suggesting the immense amount of hydrogen fuel generation, however, due to the current detection limit of our laboratory-scale instrument, the LSV curves for the large size electrode becomes saturated once the current is reached to 350-380 mA. The optical image in Supplementary Fig. 19g shows the working photograph of 5cm*5cm NiP₂-FeP₂/Cu_{NW}/Cu_f ring electrode generating hydrogen gas bubbles at -0.2 V vs. RHE (iR-uncorrected), corroborating its chance for large scale industrial application.

Theoretical investigation of the intrinsic catalytic activity. To deeply understand the intrinsic factors responsible for the outstanding HER performance of the designed NiP₂-FeP₂/Cu_{NW}/Cu_f heterointerface electrocatalyst, density functional theory (DFT) calculations were performed to

establish the HER Gibbs free energy change (ΔG_{H^*}) as well as the reaction energy for water splitting in alkaline conditions of four different surfaces: NiP₂, FeP₂, the interface-rich NiP₂-FeP₂ (NiP₂-FeP₂ IF) hybrid, and NiP₂-FeP₂ IF/Cu_{NW}. According to the finite strain theory, we constructed the NiP₂-FeP₂ IF hybrid with the most interface matching through an interface strain of 4.4%.

Generally, the Gibbs free energy for the adsorption of H* (ΔG_{H^*}) on a catalyst surface can be used as the ideal candidate to evaluate the HER activity. The computational details can be found in the method section. It is well known that to achieve the excellent performance of a good HER electrocatalyst, the absolute value of ΔG_{H^*} should be close to 0 eV. Therefore, we considered all of the possible adsorption sites and compared the ΔG_{H^*} values on the surfaces of NiP₂, FeP₂, and NiP₂-FeP₂ IF. As shown in Fig. 6a, the ΔG_{H^*} value for the NiP₂-FeP₂ IF hybrid (-0.043 eV) is much closer to the optimal value compared to those of FeP₂ and NiP₂, which had more negative ΔG_{H^*} values of -0.203 and -0.358 eV, respectively. The different adsorption sites on the surfaces with corresponding ΔG_{H^*} values are described in Figs. 6a and b, where H* adsorbed on the P site. This implies that the combination between the NiP₂ and FeP₂ could create the optimal ΔG_{H^*} and, thereafter, enhance the HER activity of the P sites at the interface. To determine the rate-determining step in alkaline media, we calculated the energy barrier for water dissociation. The energy barriers for the H₂O dissociation into the H* intermediate were found to be 0.52, 0.49, and 0.40 eV for NiP₂, FeP₂, and the NiP₂-FeP₂ IF surface, respectively (Fig. 6c and Supplementary Table 2). In fact, the significant increase of the H* source on the NiP₂-FeP₂ IF surface was attributed to the more reactive O-H bond cleavage on NiP₂-FeP₂ IF than that on NiP₂ and FeP₂, which further promotes H₂ formation. Interestingly, we found that the active sites for water dissociation mainly occurred at the interface in NiP₂-FeP₂ IF, as corroborated by the increased

charge density at the interface in NiP₂-FeP₂ IF, to form a highly catalytic active site in comparison to the NiP₂ and FeP₂ (Supplementary Figs. 20a, b, and c). Moreover, Fig. 6 and Supplementary Table 2 depict that the hybrid heterostructure between NiP₂ and FeP₂ not only approaches the optimal ΔG_{H^*} value but also provides a low energy barrier for water dissociation, thus leading to significantly enhanced HER activity compared to pristine NiP₂ and FeP₂.

Finally, we compared the HER catalytic activity of the NiP₂-FeP₂ IF hybrid with and without the Cu_{NW} support to provide a theoretical model suitable for our final designed catalyst. The most suitable site for H* adsorption on the NiP₂-FeP₂ IF/Cu_{NW} model is the P site (interface site) with a ΔG_{H^*} of -0.03 eV, which is even more optimal than that of NiP₂-FeP₂ IF, rendering it as the best HER electrocatalyst with superior performance (Figs. 6a and b). According to the differential charge density difference and Bader charge analysis, the average atomic charge for the active P site on NiP₂-FeP₂ IF/Cu_{NW} is -0.319 e^- , which is higher than that of NiP₂-FeP₂ IF hybrid (0.055 e^-) (Supplementary Figs. 20c and d). In addition, the partial density of states of the active P and H atoms on NiP₂-FeP₂ IF with/without Cu_{NW} are exhibited in Fig. 6d. We calculated the p-band center of the active P atom, which may be helpful to describe the binding strength of active P sites and the reactants. We suggest that the Cu_{NW} support leads to an upshift of the p-band center to a lower energy level, thereby decreasing the binding strength of H*, which can explain the easy desorption of H* on the P site of NiP₂-FeP₂ IF/Cu_{NW}. Importantly, we found an extremely low energy barrier for water dissociation, which is only 0.16 eV for the NiP₂-FeP₂ IF/Cu_{NW} hybrid catalyst and agrees with the experimentally observed HER performance trends under alkaline media (Fig. 6c). Therefore, the DFT calculations reveal that the role of the Cu_{NW} is not only limited

to the increase of the charge transfer from the Cu substrate to P sites favorable for H* desorption but also facilitates the water dissociation with much lower transition states energy barrier.

Based on the above theoretical investigation (DFT calculation) and experimental results, we proposed an optimized mechanistic pathway for further understanding the catalytic alkaline HER mechanism (Fig. 6e). According to the experimental Tafel slope of the NiP₂-FeP₂/Cu_{NW}/Cu_f in the alkaline medium, the hydrogen molecule is released through the Heyrovsky reaction. It is already well studied that in alkaline media, the catalytic dissociation of the H₂O molecule to generate H* is the first sluggish Volmer step ($\text{H}_2\text{O} + e^- = \text{H}^* + \text{OH}^-$). Interestingly from our calculation results, we found that the active site for water dissociation mainly occurred at the interface in NiP₂-FeP₂ IF with the most energetic favorable configuration of H₂O molecule adsorbed on the top of Ni site. Thus, the interface is found to be more active toward water dissociation. The catalytic cycle is initiated by activation of the H₂O molecule onto the Ni site (step-I), followed by dissociation into H* and OH* species adsorbed on the nearby P and Ni, respectively, (step-II). Eventually, another proton from the adjacent H₂O molecule reacts with the adsorbed H* and generate molecular H₂ (step-III-IV-V), in-turn regenerating the active sites.

Overall water splitting with NiP₂-FeP₂/Cu_{NW}/Cu_f (-) || NiFe-LDH/Ni_f (+) catalysts. To evaluate the possibility of utilizing the hybrid NiP₂-FeP₂/Cu_{NW}/Cu_f electrode for large-scale hydrogen production, we carried out overall water splitting test in a two-electrode configuration with the NiP₂-FeP₂/Cu_{NW}/Cu_f electrode as the cathode and high-performance NiFe-LDH/Ni_f as the anode in 1 M KOH. Supplementary Fig. 21 shows that the superior OER performance of the NiFe-LDH/Ni_f electrode is even better than that of state-of-the-art RuO₂ and the NiFe-LDH/ Cu_{NW}/Cu_f electrode in 1 M KOH. As shown in Figs. 7a and b, the NiP₂-FeP₂/Cu_{NW}/Cu_f (-) || NiFe-LDH/Ni_f (+) electrolyzer demands an extremely low cell voltage of only 1.42 V at 10 mA cm⁻² with a rapidly

increasing current density with bias voltage, suggesting an electrical-to-fuel efficiency of 86.6%. The performance of the NiP₂-FeP₂/Cu_{NW}/Cu_f (-) || NiFe-LDH/Ni_f (+) electrolyzer is even superior to that of the Pt/C/Cu_f (-) || RuO₂/Ni_f (+) electrolyzer, which needs 1.5 V to attain 10 mA cm⁻². This performance is also superior to that of the 20 Wt% Pt/C/Cu_f (-) || NiFe-LDH/Ni_f (+) electrolyzer, demonstrating the superior HER performance of our NiP₂-FeP₂/Cu_{NW}/Cu_f electrode compared to commercial Pt/C (Supplementary Fig. 22). This cell voltage is superior to most previously reported alkaline electrolyzers, which generally require more than 1.45 V at the same current density (Supplementary Table 3). The chronopotentiometry test in Fig. 7c reveals the superior stability of the designed electrolyzer at a high current density of 500 mA cm⁻² for at least 60 h with continuous release of oxygen and hydrogen gas bubbles at the respective electrode (Supplementary Video 1). Also, in the Supplementary Video 1 recorded at 2.5 V (@ 500 mA cm⁻²) cell voltage, the hydrogen bubbles are smoothly released from our HER electrode, corroborating the absence of any bubble accumulation signature during the long term stability test. Meanwhile, the Pt/C/Cu_f (-) || RuO₂ (+)/Ni_f electrolyzer shows relatively poor stability at the same current density, limiting its commercial application with respect to the former. The above results suggest that the hybrid NiP₂-FeP₂/Cu_{NW}/Cu_f electrode can be a suitable replacement for the benchmarking Pt/C electrode for efficient alkaline electrolyzers with an exceptionally low overpotential for water splitting systems.

Electrolysis and photolysis of seawater at elevated temperatures. Considering the scarcity of the freshwater supply on earth along with costly desalination steps, direct splitting of earth-abundant seawater using solar energy will make the water splitting system highly economical for generating hydrogen fuel.⁴¹ In this regard, we first investigated the OER and HER performance of NiFe-LDH/Ni_f and NiP₂-FeP₂/Cu_{NW}/Cu_f electrode, respectively, under an artificial seawater-based

electrolyte (0.6 M NaCl in 1 M KOH) and compared with 20 Wt% Pt/C/Cu_f (Supplementary Fig. 23). The NiFe-LDH/Ni_f and NiP₂-FeP₂/Cu_{NW}/Cu_f electrode also show superior performance towards OER and HER, respectively, under artificial seawater-based electrolyte. Inspired from the high HER and OER performance under seawater based electrolyte, we investigated the full water splitting performance of the NiP₂-FeP₂/Cu_{NW}/Cu_f (-) || NiFe-LDH/Ni_f (+) electrolyzer under the artificial seawater-based electrolyte at 25 °C and 100 °C. As shown in Figs. 8a and b, the NiP₂-FeP₂/Cu_{NW}/Cu_f (-) || NiFe-LDH/Ni_f (+) electrolyzer attains a current density of 10 mA cm⁻² at cell voltages of only 1.4 and 1.31 V at 25 °C and 100 °C, respectively, in artificial seawater with a rapidly increasing current density up to 1 A cm⁻² at a cell voltage of only 2.63 V at 100 °C, which is suitable from the practical point of view. This performance is also superior to that of the 20 Wt% Pt/C/Cu_f (-) || NiFe-LDH/Ni_f (+) electrolyzer under same electrolyte condition (Supplementary Fig. 24a, b). This cell voltage for a seawater-based electrolyte is the lowest reported value for a water-splitting device (Supplementary Table 3). The NiP₂-FeP₂/Cu_{NW}/Cu_f (-) || NiFe-LDH/Ni_f (+) electrolyzer also shows superior performance under 1 M KOH in real seawater (Supplementary Fig. 24c, d). The stability test under seawater at 25 °C shows that the electrolyzer is fairly stable for 275 h at 100 mA cm⁻² without any noticeable decrease of the current density. For practical applications, the durability at an extremely high current density of 1200 mA cm⁻² was also investigated, and the electrolyzer showed superior stability for at least 30 h with the vigorous release of gas bubbles (Fig. 8c).

One of the biggest challenges associated with the seawater splitting is the stoichiometry of the H₂ and O₂ production, which is generally hampered due to the presence of the non-negligible amount of Cl⁻ ions, making oxidation of chlorine as a major obstacle for the anodic OER process. At lower pH below 3, the free Cl₂ evolution reaction is dominant, whereas, at high pH range (7.5

to 14), due to the high solubility of the Cl_2 in aqueous solution, the major competitive anodic reaction is hypochlorous acid (HOCl) and hypochlorite ions (OCl^-) formation along with OER, however rapidly evolved Cl_2 could still be released from the electrolyte.⁴² To address these concerns over probable Cl_2 evolution or hypochlorous acid/hypochlorite ion formation, we carried out o-tolidine test to examine the presence of hypochlorous acid/hypochlorite ion in the artificial seawater electrolyte as well as gas chromatography (GC) to analyze the gaseous product collected after the seawater electrolysis test using our $\text{NiP}_2\text{-FeP}_2/\text{Cu}_{\text{NW}}/\text{Cu}_{\text{f}}$ (-) || $\text{NiFe-LDH}/\text{Ni}_{\text{f}}$ (+) electrolyzer. Supplementary Fig. 25a shows the chemical reaction between the o-tolidine and HClO/NaOCl . Supplementary Fig. 25b, c shows the UV-vis spectra of the testing solution with different amounts of Cl_2 and the corresponding calibration curve obtained by plotting the concentration of free chlorine against the corresponding absorption peak, respectively, whereas, Supplementary Fig. 25d, e shows the UV-vis spectra of the testing solution with different amounts of NaOCl and the corresponding calibration curve obtained by plotting the concentration of free OCl^- against the corresponding absorption peak, respectively.^{43,44} As revealed in Supplementary Fig. 25f, our electrolyzer did not generate any traceable amount of HClO/OCl^- ions in the electrolyte even after 1 h of continuous testing at a cell voltage of 2.6 V. The GC data also suggest that only O_2 and H_2 (nitrogen is used for purging the electrolyte/atmosphere) are the detectable gas-phase products generated from our electrolyzer, further affirming the superior selectivity of our electrolyzer towards seawater splitting (Supplementary Fig. 25f inset). Furthermore, faradaic efficiency of our electrolyzer in artificial seawater was evaluated by collecting the actual amount of H_2 and O_2 gas evolved over the cathode and anode, respectively, operated at 2.6 V. Both $\text{NiFe-LDH}/\text{Ni}_{\text{f}}$ and $\text{NiP}_2\text{-FeP}_2/\text{Cu}_{\text{NW}}/\text{Cu}_{\text{f}}$ electrodes demonstrate near 100% faradaic efficiency (99.3% for O_2 and 99.2% for H_2), with a stoichiometric H_2 : O_2 ratio of 2:1 (Supplementary Fig. 25g, h).

With a goal to develop a solar-energy-driven seawater photolyzer with a high STH efficiency for remote locations that have a limited supply of electricity, a commercial Si solar cell was employed to harness solar energy directly to electricity to split seawater using the NiP₂-FeP₂/Cu_{NW}/Cu_f (-) || NiFe-LDH/Ni_f (+) electrolyzer, as schematically illustrated in Fig. 9a. Fig. 9b shows the J-V characteristic curve of the commercial Si solar cell in the dark and under 100 mW cm⁻² illumination, demonstrating a short-circuit photocurrent density, open-circuit voltage, and fill factor of 17.22 mA cm⁻², 2.275 V, and 0.677, respectively, yielding a power conversion efficiency (PCE) of 26.53%. When this solar cell is connected with the electrolyzer, a high photocurrent density of 17 mA cm⁻² is generated via seawater photolysis at 100 °C, corresponding to a high STH conversion efficiency of 19.85% (considering that the thermodynamic potential for the water-splitting reaction is 1.168 V at 100 °C) under 1 sun illumination, assuming the faradaic efficiency to be 100% based on the long term stability test under seawater (Fig. 9c). This STH value is one of the highest reported values to date for seawater photolysis (Supplementary Table 4). Because of the exceptional stability of the electrolyzer under seawater, the device can maintain the same photocurrent density for a longer duration (45 min), as confirmed from the unbiased light-driven configuration measurement in Fig. 9d under chopped light illumination without any external bias. The optical images in Figs. 9e, f, and g show the generation of hydrogen and oxygen gas bubbles at the respective electrodes under the illumination of the solar cell connected to the electrolyzer (Supplementary Video 2). Such a high STH value demonstrates that pairing of the designed NiP₂-FeP₂/Cu_{NW}/Cu_f HER electrode with the NiFe-LDH anode can be employed for real, large-scale hydrogen generation from seawater using direct sunlight.

Conclusions

In summary, we demonstrated a simple and cost-effective approach for the fabrication of a highly active and stable self-supported HER electrode, NiP₂-FeP₂/Cu_{NW}/Cu_f, which demonstrated performance superior to the state-of-the-art Pt/C under alkaline conditions. The as-prepared NiP₂-FeP₂/Cu_{NW}/Cu_f hybrid electrode exhibited an extremely low overpotential of only 23.6 mV to reach a current density of -10 mA cm⁻², outperforming the commercial 20 wt% Pt/C/Cu_f electrode ($\eta^{10} = 32$ mV). The HER current density increases rapidly and achieves current commercial densities of -500 and -1,000 mA cm⁻² at overpotentials of only 323 and 357 mV, respectively, with outstanding stability at the industrial current density of -1 A cm⁻². Theoretical calculations reveal that the introduction of the Cu_{NW} support to the interface-rich NiP₂-FeP₂ significantly lowered the water dissociation barrier with a value of only 0.16 eV as well as close to zero H adsorption energy (-0.03 eV), thereby boosting the HER performance. Further, the superior mechanical and electrical contact between the active NiP₂-FeP₂ and the conducting Cu core anchored on the Cu substrate along with numerous exposed active sites for better mass diffusion synergistically enhances the HER performance. The electrolyzer constructed by pairing this HER electrode with the NiFe-LDH anode achieved a current density of 10 mA cm⁻² at cell voltages of 1.42, 1.4, and 1.31 V under 1 M KOH, 1 M KOH with 0.6 M NaCl (artificial seawater-25 °C), and artificial seawater-100 °C, respectively, along with superior stability at a high current density. When connected to the Si solar cell for remote locations with limited electricity, this device generated an STH conversion efficiency of 19.85% under seawater at 100 °C, demonstrating the possibility for commercial large-scale hydrogen production. Thus, our new design concept “Interface-active electrode” is not only limited to hydrogen generation, rather can also be extended to the other fields of materials science and catalysis (such as catalyst for CO₂/N₂/O₂ reduction reactions and so on).

Methods.

Chemicals. Ammonium persulfate ($(\text{NH}_4)_2\text{S}_2\text{O}_8$; Sigma-Aldrich, $\geq 98\%$), sodium hydroxide (NaOH; Samchun, 97%), nickel(II) nitrate hexahydrate ($\text{Ni}(\text{NO}_3)_2 \cdot 6\text{H}_2\text{O}$; Sigma-Aldrich, $\geq 99\%$), iron(III) nitrate nonahydrate ($\text{Fe}(\text{NO}_3)_3 \cdot 9\text{H}_2\text{O}$; Sigma-Aldrich, $\geq 99\%$), sodium bicarbonate (NaHCO_3 ; Sigma-Aldrich, $\geq 99.7\%$), sodium hypophosphite monohydrate ($\text{NaH}_2\text{PO}_2 \cdot \text{H}_2\text{O}$; Sigma-Aldrich, $\geq 99\%$), potassium hydroxide pellets (KOH; Sigma-Aldrich, $\geq 85\%$), ethanol ($\text{C}_2\text{H}_5\text{OH}$; Sigma-Aldrich, $\geq 99.9\%$), Toray carbon fiber paper/Cu foam/Ni foam (Alfa Aesar), and the nafion perfluorinated resin solution (5 wt %, Sigma-Aldrich) were used without further purification.

Synthesis of metallic copper nanowire on Cu foam ($\text{Cu}_{\text{NW}}/\text{Cu}_f$): The growth of metallic Cu_{NW} involves three steps. First, copper hydroxide ($\text{Cu}(\text{OH})_2$) nanowires were grown on the Cu foam via a chemical oxidation method. During synthesis, a piece of copper foam (0.5cm*0.6cm and thickness 0.5mm) was cleaned in hydrochloric acid (37% HCl) followed by sonication in ethanol and deionized water for 15 min sequentially. After the cleaning process, the Cu foam was immersed into 14 mL of an aqueous solution containing 300 mg of $(\text{NH}_4)_2\text{S}_2\text{O}_8$ and 1.05 g of NaOH for 30 min. Then, the Cu foam with a light blue color was washed multiple times with deionized water and dried in the open air. Following the synthesis of $\text{Cu}(\text{OH})_2$ nanowires on the Cu foam, the nanowires were converted into CuO nanowires by calcining at 180 °C for 1 h. Finally, the CuO nanowires were electrochemically reduced to metallic Cu nanowires on the Cu foam at -1.08 V vs. Ag/AgCl in an Ar-saturated 1 M NaHCO_3 solution.

Synthesis of NiFe-LDH on $\text{Cu}_{\text{NW}}/\text{Cu}_f$: The NiFe-LDH was electrodeposited on Cu_{NW} in a typical three-electrode configuration using $\text{Cu}_{\text{NW}}/\text{Cu}_f$ as the working electrode, Pt mesh as the counter electrode, and Ag/AgCl as the reference electrode. The electrodeposition was carried out at -1.2 V vs. Ag/AgCl for different electrodeposition times (30, 60, and 90 s) in an electrolyte containing 0.04 M $\text{Ni}(\text{NO}_3)_2 \cdot 6\text{H}_2\text{O}$ and 0.04 M $\text{Fe}(\text{NO}_3)_3 \cdot 9\text{H}_2\text{O}$ in 50 mL water and denoted as NiFe-LDH/ $\text{Cu}_{\text{NW}}/\text{Cu}_f$. Then, the samples were washed with deionized water several times and dried in air. For comparison, NiFe-LDH samples with different ratios of Ni: Fe (1:2 and 2:1) were synthesized by varying the ratio of $\text{Ni}(\text{NO}_3)_2 \cdot 6\text{H}_2\text{O}$ and $\text{Fe}(\text{NO}_3)_3 \cdot 9\text{H}_2\text{O}$ using the above method. Also, for comparison, NiFe-LDH on commercial carbon fiber paper was also synthesized via the same method and denoted as NiFe-LDH/CFP.

Synthesis of $\text{NiP}_2\text{-FeP}_2$ on $\text{Cu}_{\text{NW}}/\text{Cu}_f$: The NiFe-LDH/ $\text{Cu}_{\text{NW}}/\text{Cu}_f$ was thermally phosphorized via a vapor phase phosphidation process in the tube furnace to obtain $\text{NiP}_2\text{-FeP}_2$ on $\text{Cu}_{\text{NW}}/\text{Cu}_f$, denoted as $\text{NiP}_2\text{-FeP}_2/\text{Cu}_{\text{NW}}/\text{Cu}_f$. During synthesis, the obtained NiFe-LDH/ $\text{Cu}_{\text{NW}}/\text{Cu}_f$ was placed on the downstream side, whereas the phosphorus source, $\text{NaH}_2\text{PO}_2 \cdot \text{H}_2\text{O}$, was placed on the upstream side of the surface. Both zones of the furnace were heated up to 350 °C with a heating rate of 3 °C min^{-1} and held at that temperature for 2 h under continuous Ar flow. Finally, the furnace was

naturally cooled down to room temperature under Ar flow (loading: 0.8 mg cm^{-2}). For comparison, $\text{NiP}_2\text{-FeP}_2$ 1:2/ $\text{Cu}_{\text{NW}}/\text{Cu}_f$ and $\text{NiP}_2\text{-FeP}_2$ 2:1/ $\text{Cu}_{\text{NW}}/\text{Cu}_f$ were also synthesized following the same procedure by using the other two ratios of the NiFe-LDH synthesized above. Additionally, for comparison, $\text{NiP}_2\text{-FeP}_2$ was also synthesized on commercial carbon fiber paper ($\text{NiP}_2\text{-FeP}_2/\text{CFP}$) via the same procedure (loading: 0.77 mg cm^{-2}).

Synthesis of NiFe-LDH on Ni foam: The NiFe-LDH was electrodeposited on Ni foam in a typical three-electrode configuration using Ni foam as the working electrode, Pt mesh as the counter electrode, and Ag/AgCl as the reference electrode. The electrodeposition was carried out at -1.2 V vs. Ag/AgCl for 250 s in an electrolyte containing $0.04 \text{ M Ni}(\text{NO}_3)_2 \cdot 6\text{H}_2\text{O}$ and $0.04 \text{ M Fe}(\text{NO}_3)_3 \cdot 9\text{H}_2\text{O}$ in 50 mL water, denoted as NiFe-LDH/ Ni_f . The samples were then washed with deionized water several times and dried in air (loading: 1.5 mg cm^{-2}).

Material characterization: FESEM images were obtained using a JEOL 7500F FESEM. The EDS spectra were recorded in an Oxford Instruments X-Max with the INCA software coupled to the FESEM. TEM images were recorded using a JEOL JEM-2100F. The powder XRD measurements were performed using a Rigaku Ultima IV powder X-ray diffractometer. The X-ray photoelectron spectroscopy (XPS) measurements were performed on a Thermo VG Microtech ESCA 2000, with a monochromatic Al-K α X-ray source at 100 W. Argon ion etching was done for 60 sec. The acquired data were background corrected by the Shirley method, and the peaks were fitted using Fityk software, with Voigt peaks containing 80% Gaussian and 20% Lorentzian components to find the valence states. XANES and EXAFS analyses were conducted with a BL 10C beam line at Pohang Light Source (Korea) operated at 3.0 GeV with a 200-mA ring current. UV-vis data were obtained using a UV-vis spectrophotometer (Jasco, V-670 in Spain) operating at ambient conditions. GC measurements were conducted using the 7890A GC system, Agilent Technologies, USA, instrument.

Electrochemical measurements: All of the electrochemical measurements were carried out using a VMP3 electrochemical workstation (Bio-logic Science Instruments, France) in a conventional three-electrode system and the overall water splitting test was carried out in a two-electrode configuration in 1 M KOH as well as with the addition of 0.6 M NaCl to emulate seawater. The synthesized self-supported electrodes were directly used as the working electrode, Pt mesh as the counter electrode, and Ag/AgCl (3 M KCl) as the reference electrode. For commercial Pt/C and RuO_2 , the ink was prepared by dispersing 5 mg of powder in 500 mL of ethanol containing 20 mL 5% Nafion and sonicated for 60 min. The catalyst ink was drop-cast onto Cu foam in the case of Pt/C (loading: 0.8 mg cm^{-2}) and onto Ni foam for RuO_2 (loading: 1.5 mg cm^{-2}) and left to dry in air. All of the working electrodes were saturated using

cyclic voltammetry (CV) scans at a scan rate of 100 mV s⁻¹ before performing the measurements. The LSV polarization curve was obtained at a scan rate of 10 mV s⁻¹ to minimize the capacitive current and at an even slower scan rate of 5 mV s⁻¹ for some specific catalysts.⁴⁵ EIS spectra were measured in the faradaic region to compare the charge transfer resistance among different catalysts (R_{CT}). C_{dl} was obtained by collecting CVs at various scan rates of 10, 30, 50, 70, and 90 mV s⁻¹ in the non-faradaic region (0.77 to 0.87 V vs. RHE). ECSA was obtained from the C_{dl} value using a specific capacitance of 0.04 mF/cm². All of the potentials referred to the Ag/AgCl were converted to the reversible hydrogen electrode using the Nernst equation.

$$E_{(RHE)} = E_{(Ag/AgCl)} + E^0_{(Ag/AgCl)} + 0.059 \times \text{pH}$$

The long-term stability test was performed by chronopotentiometry. All of the potentials in the three-electrode configuration were 85% iR-corrected with respect to the ohmic resistance of the solution unless specified and calibrated to the RHE using the following equation.

$$E_{(RHE)} = E_{(Ag/AgCl)} + E^0_{(Ag/AgCl)} + 0.059 \times \text{pH} - 85\% \text{ iRs}$$

For water photolysis using direct sunlight, a commercial Si solar cell with an efficiency of 26.53% was employed and connected with the electrolyzer in series. The current of the water photolysis was recorded by chronoamperometry under AM 1.5G illumination without applying any external bias.

Computational details: All DFT calculations were carried out using the projected augmented wave (PAW) pseudopotentials method^{46,47} and Perdew-Burke-Ernzerhof generalized gradient exchange approximation (PBE-GGA) correlational functional⁴⁸ as implemented in the VASP package.⁴⁹ Spin-polarized calculations were performed using the Van der Waals correction at the Grimme-D3 level⁵⁰ for both geometry optimization and zero-point energy-free energies (ZPE). The cut-off energy of 400 eV was chosen for the calculations. The total energy was smaller than 10⁻⁴ eV/cell, and the force convergence criterion was set to -0.01 eV/Å with a vacuum layer of 15 Å for lattice circulation to eliminate the interaction between two periodic images.

The catalytic structures were modeled by five-layered NiP₂ and FeP₂ with space groups of PA-3 and Pnm, respectively. The NiP₂-FeP₂ IF hybrid model was built in (2x2) NiP₂ (210) and (2x2) FeP₂ (101), which provided a small interfacial strain of 4.4%. For the NiP₂-FeP₂ IF/Cu_{NW} support, the NiP₂-FeP₂ IF hybrid was reduced on Cu (111) consisting of 144 atoms.

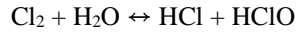
The free energy change for H* adsorption was calculated as follows: -

$$\Delta G_{H^*} = E_{[*+H]} - E_{[*]} - \frac{1}{2} E_{[H_2]} + \Delta E_{ZPE} - T\Delta S_H$$

where $E_{[*+H]}$ and $E_{[*]}$ are the total energies of the surface with and without H adsorption, respectively, $E_{[H_2]}$ is the total energy of the H_2 molecule in the gas phase, and ΔE_{ZPE} and ΔS_H are the zero-point energy change and entropy change of H adsorption, respectively.

To determine the transition state for water dissociation, we employed the climbing image nudged elastic band (CI-NEB) method. The force component perpendicular to each atom in the search reaction pathway was set to 0.01 eV Å⁻¹. The initial (H_2O^*) and final (H^* and OH^*) states were found after relaxing multiple possible locations on these surfaces. Finally, to understand the charge transfer process between NiP_2 - FeP_2 and Cu_{NW} , the Bader charges of each compound were calculated.

Chlorine determination by o-tolidine: The free chlorine is highly soluble in water and undergoes reaction with water to generate hydrochloric acid (HCl) and hypochlorous acid (HClO), according to the following equation:



Also, at higher pH, another possible competitive anodic reaction is the hypochlorite formation (ClO^-), according to the following equation:



In order to affirm the selectivity of our electrolyzer, o-tolidine tests were performed because HClO is difficult to isolate from the electrolyte due to its rapid equilibrium with water and Cl_2 . However it undergoes redox reaction with o-tolidine and can be detected (Supplementary Fig. 25a). The testing solution contained 10 mL of deionized water and 0.5 mL of o-tolidine solution (0.05M in ethanol). To obtain the calibration curve for Cl_2 , different amounts of freshly prepared Cl_2 generated (10, 20, 30, 40, and 50 μ L) by mixing 1 g of $KMnO_4$ and 10 mL of concentrated HCl in a sealed vial for 10 min was injected into the testing solution. The seawater electrolysis experiment was carried out in 50 mL of 1M KOH + 0.6 M NaCl electrolyte using NiP_2 - FeP_2 / Cu_{NW} / Cu_f (-) || $NiFe$ -LDH/ Ni_f (+) electrolyzer at different cell voltages. 0.2 mL of the electrolyte was collected after the electrolysis and then added into the testing solution. For the determination of hypochlorite ion, standard NaOCl was used for detection. For the calibration of ClO^- , the different molar amount of NaOCl (5.96, 11.92, 17.89, 23.85, 29.82 μ mol) was injected to the testing solution.⁴¹

References

1. Turner, J. A. Sustainable hydrogen production. *Science* **305**, 972–974 (2004).
2. Luo, J. et al. Water photolysis at 12.3% efficiency via perovskite photovoltaics and Earth-abundant catalysts. *Science* **345**, 1593–1596 (2014).
3. Ling, T. et al. Activating cobalt (II) oxide nanorods for efficient electrocatalysis by strain engineering. *Nat. Commun.* **8**, 1509 (2017).
4. Zhou, H. Q. et al. Efficient hydrogen evolution by ternary molybdenum sulfoselenide particles on self-standing porous nickel diselenide foam. *Nat. Commun.* **7**, 12765 (2016).
5. Kuang, Y. et al. Solar-driven, highly sustained splitting of seawater into hydrogen and oxygen fuels. *PNAS* **116**, 6624–6629 (2019).
6. Yu, F. et al. High-performance bifunctional porous non-noble metal phosphide catalyst for overall water splitting. *Nat. Commun.* **9**, 2551 (2018).
7. Seitz, L. C. et al. A highly active and stable $\text{IrO}_x/\text{SrIrO}_3$ catalyst for the oxygen evolution reaction. *Science* **353**, 1011–1014 (2016).
8. Lu, B. et al. Ruthenium atomically dispersed in carbon outperforms platinum toward hydrogen evolution in alkaline media. *Nat. Commun.* **10**, 631 (2019).
9. Yin, J. et al. Oxygen vacancies dominated $\text{NiS}_2/\text{CoS}_2$ interface porous nanowires for portable Zn–air batteries driven water splitting devices. *Adv. Mater.* **29**, 1704681 (2017).
10. Dinh, C. T. et al. Multi-site electrocatalysts for hydrogen evolution in neutral media by destabilization of water molecules. *Nat. Energy* **4**, 107–114 (2019).
11. Kumar, A. & Bhattacharyya, S. Porous NiFe-oxide nanocubes as bifunctional electrocatalysts for efficient water-splitting. *ACS Appl. Mater. Interfaces*, **9**, 41906–41915 (2017).
12. Jaramillo, T. F. et al. Identification of active edge sites for electrochemical H_2 evolution from MoS_2 nanocatalysts. *Science* **317**, 100–102 (2007).
13. Tian, J., Liu, Q., Asiri, A. M. & Sun, X. Self-supported nanoporous cobalt phosphide nanowire arrays: an efficient 3D hydrogen-evolving cathode over the wide range of pH 0–14. *J. Am. Chem. Soc.* **136**, 7587–7590 (2014).
14. Zheng, Y. R. et al. Doping-induced structural phase transition in cobalt diselenide enables enhanced hydrogen evolution catalysis. *Nat. Commun.* **9**, 2533 (2018).
15. Lin, H. et al. Heteronanowires of $\text{MoC-Mo}_2\text{C}$ as Efficient Electrocatalysts for Hydrogen Evolution Reaction. *Chem. Sci.* **7**, 3399–3405 (2016).
16. Xie, L. et al. *In situ* formation of a 3D core/shell structured $\text{Ni}_3\text{N@Ni-Bi}$ nanosheet array: an efficient nonnoble-metal bifunctional electrocatalyst toward full water splitting under near-neutral conditions. *J. Mater. Chem. A*, **5**, 7806–7810 (2017).
17. Kumar, A., Chaudhary, D. K., Parvin, S. & Bhattacharyya, S. High performance duckweed-derived carbon support to anchor NiFe electrocatalysts for efficient solar energy driven water splitting. *J. Mater. Chem. A*, **6**, 18948–18959 (2018).
18. Jothi, V. R., Bose, R., Rajan, H., Jung, C. & Yi, S. C. Harvesting electronic waste for the development of highly efficient eco-design electrodes for electrocatalytic water splitting. *Adv. Energy Mater.* **8**, 1802615 (2018).
19. Cheng, L., Zhang, D., Fan, J., Liao, Y. & Xiang, Q. Metal phosphide modified $\text{Cd}_x\text{Zn}_{1-x}\text{S}$ solid solutions as a highly active visible-light photocatalyst for hydrogen evolution. *Applied Catalysis A: General* **590**, 117336 (2020).
20. Zhang, H., Zhou, W., Dong, J., Lu, X. F. & Lou, X. W. Intramolecular electronic coupling in porous iron cobalt (oxy)phosphide nanoboxes enhances the electrocatalytic activity for oxygen evolution. *Energy Environ. Sci.* **12**, 3348–3355 (2019).
21. Xu, J. et al. Boosting the hydrogen evolution performance of ruthenium clusters through synergistic coupling with cobalt phosphide. *Energy Environ. Sci.* **11**, 1819–1827 (2018).
22. Song, B. et al. Tuning mixed nickel iron phosphosulfide nanosheet electrocatalysts for enhanced hydrogen and

- oxygen evolution. *ACS Catal.* **7**, 8549-8557 (2017).
23. Parvin, S., Kumar, A., Ghosh, A. & Bhattacharyya, S. An earth-abundant bimetallic catalyst coated metallic nanowire grown electrode with platinumlike pH-universal hydrogen evolution activity at high current density. *Chem. Sci.* **11**, 3893–3902 (2018).
 24. Mahmood, J. et al. An efficient and pH-universal ruthenium-based catalyst for the hydrogen evolution reaction. *Nat. Nano.* **12**, 441–446 (2017).
 25. Al Cheikh, J., Villagra, A., Ranjbari, A., Pradon, A., Antuch, M., Dragoe, D., Millet, P. & Assaud, L. Engineering a cobalt clathrochelate/glassy carbon interface for the hydrogen evolution reaction. *Applied Catalysis B: Environmental* **250**, 292-300 (2019).
 26. Yu, F., Yao, H., Wang, B., Zhang, K., Zhang, Z., Xie, L., Hao, J., Mao, B., Shen, H. & Shi, W. Nickel foam derived nitrogen doped nickel sulfide nanowires as an efficient electrocatalyst for the hydrogen evolution reaction. *Dalton Transactions* **47**, 9871-9876 (2018).
 27. Feng, J. X. et al. FeOOH/Co/FeOOH hybrid nanotube arrays as high-performance electrocatalysts for the oxygen evolution reaction. *Angew. Chem.* **128**, 3758–3762 (2016).
 28. Yu, L. et al. Cu nanowires shelled with NiFe layered double hydroxide nanosheets as bifunctional electrocatalysts for overall water splitting. *Energy Environ. Sci.* **10**, 1820–1827 (2017).
 29. Xu, P., Ye, K., Du, M., Liu, J., Cheng, K., Yin, J., Wang, G. & Cao, D. One-step synthesis of copper compounds on copper foil and their supercapacitive performance. *RSC Adv.* **5**, 36656-36664 (2015).
 30. Dung Dang, T., Tuyet Le, T., Fribourg-Blanc, E. & Chien Dang, M. The influence of solvents and surfactants on the preparation of copper nanoparticles by a chemical reduction method. *Advances in Natural Sciences: Nanoscience and Nanotechnology* **2**, 025004 (2011).
 31. Cao, Q., Wang, C., Chen, S., Xu, X., Liu, F., Geng, X., & Wang, J. Vertically aligned NiP₂ nanosheets with interlaced mesh network for highly efficient water splitting under alkaline and acid solutions. *Int J Hydrogen Energy* **44**, 6535-6543 (2019).
 32. Jiang, J. et al. Synthesis of FeP₂/C nanohybrids and their performance for hydrogen evolution reaction. *J. Mater. Chem. A* **3**, 499–503 (2015).
 33. Tahir, D. & Tougaard, S. Electronic and optical properties of Cu, CuO and Cu₂O studied by electron spectroscopy. *J. Phys: Cond. Matt.* **24**, 175002 (2012).
 34. Wei, S., Qi, K., Jin, Z., Cao, J., Zheng, W., Chen, H. & Cui, X. One-step synthesis of a self-supported copper phosphide nanobush for overall water splitting. *ACS Omega* **1**, 1367–1373 (2016).
 35. Zhang, C., Xie, Y., Deng, H., Zhang, C., Su, J. W., Dong, Y. & Lin, J. Ternary nickel iron phosphide supported on nickel foam as a high-efficiency electrocatalyst for overall water splitting. *Int J Hydrogen Energy* **43**, 7299-7306 (2018).
 36. Fomina, M. et al. Role of oxalic acid overexcretion in transformations of toxic metal minerals by *Beauveria caledonica*. *Appl. Environ. Microbiol.* **71**, 371–381 (2005).
 37. Wang, X., Pi, M., Zhang, D., Li, H., Feng, J., Chen, S. & Li, J. Insight into the Superior Electrocatalytic Performance of a Ternary Nickel Iron Poly-Phosphide Nanosheet Array: An X-ray Absorption Study. *ACS Appl. Mater. Interfaces.* **11**, 14059–14065 (2019).
 38. Silva, D. C. C., Crosnier, O., Ouvrard, G., Greedan, J., Safa-Sefat, A. & Nazar, L. F. Reversible Lithium Uptake by FeP₂. *Electrochem. Solid-State Lett.* **6**, A162-A165 (2003).
 39. Cao, Z., Chen, Q., Zhang, J., Li, H., Jiang, Y., Shen, S., Fu, G., Lu, B., Xie, Z. & Zheng, L. Platinum-nickel alloy excavated nano-multipods with hexagonal close-packed structure and superior activity towards hydrogen evolution reaction. *Nat Comm.* **8**, 15131 (2017).
 40. Chen, Z., Cummins, D., Reinecke, B., Clark, E., Sunkara, M. & Jaramillo, T. Core-shell MoO₃-MoS₂ nanowires for hydrogen evolution: a functional design for electrocatalytic materials. *Nano Lett.* **11**, 4168-4175 (2011).
 41. Karagiannis, I. C. & Petros G. Soldatos, P. G. Water desalination cost literature: review and assessment. *Desalination.* **223**, 448-456 (2008).
 42. Tong, W., Forster, M., Dionigi, F., Dresch, S., Erami, R. S., Strasser, P., Cowan, A. J. & Farràs, P. Electrolysis of

- low-grade and saline surface water. *Nat Energy*, DOI: 10.1038/s41560-020-0550-8 (2020).
43. Hsu, S. H. et al. An earth-abundant catalyst-based seawater photoelectrolysis system with 17.9% solar-to-hydrogen efficiency. *Adv. Mater.* **30**, 1707261 (2018).
 44. Graham, H. D. Ortho-Tolidine and Sodium Hypochlorite for the Determination of Carrageenan and Other Ester Sulfates. *J. Dairy Sci.*, **55**, 1675-1682 (1972).
 45. Debnath, B.; Kumar, A.; Salunke, H. G. & Bhattacharyya, S. Enhancing multifunctionality through secondary phase inclusion by self-assembly of Mn₃O₄ nanostructures with superior exchange anisotropy and oxygen evolution activity. *J. Phys. Chem. C* **121**, 25594-25602 (2017).
 46. Kresse, G & Joubert, D. From ultrasoft pseudopotentials to the projector augmented-wave method. *Phys. Rev. B.* **59**, 1758–1775 (1999).
 47. Blochl, P. E. Projector augmented-wave method. *Phys. Rev. B.* **50**, 17953–17979 (1994).
 48. Perdew, J. P., Burke, K. & Ernzerhof, M. Generalized gradient approximation made simple. *Phys. Rev. Lett.* **77**, 3865–3868 (1996).
 49. Kresse, G. & Hafner, J. Ab initio molecular dynamics for liquid metals. *Phys. Rev. B.* **47**, 558–561 (1993).
 50. Klimes, J., Bowler, D. R. & Michaelides, A. Van der Waals density functionals applied to solids. *Phys. Rev. B.* **83**, 195131 (2011).

Acknowledgement. This work was supported by the Institute for Basic Science (IBS-R011-D1). The authors also thank the high-performance computing support from the Institute for Materials Research (Tohoku University, Japan).

Author’s contributions. A.K designed and carried out the experiments as well as analyzed the data with support from H.L. V. Q. B. performed the theoretical calculations. J.L helped to conduct the photolysis measurements. J.W helped in collecting the FESEM images. A. R. J. helps in chlorine detection experiment. M. G. K. performed the XAS measurements. A.K, V. Q. B. and H.L co-wrote the paper. All authors have given approval to the final version.

Conflict of interest. The authors declare no competing interests.

Additional information. Additional experimental details, including FESEM images, PXRD patterns, EDAX patterns, HRTEM, electrochemical measurements, XPS, chlorine detection test and comparative tables, are available.

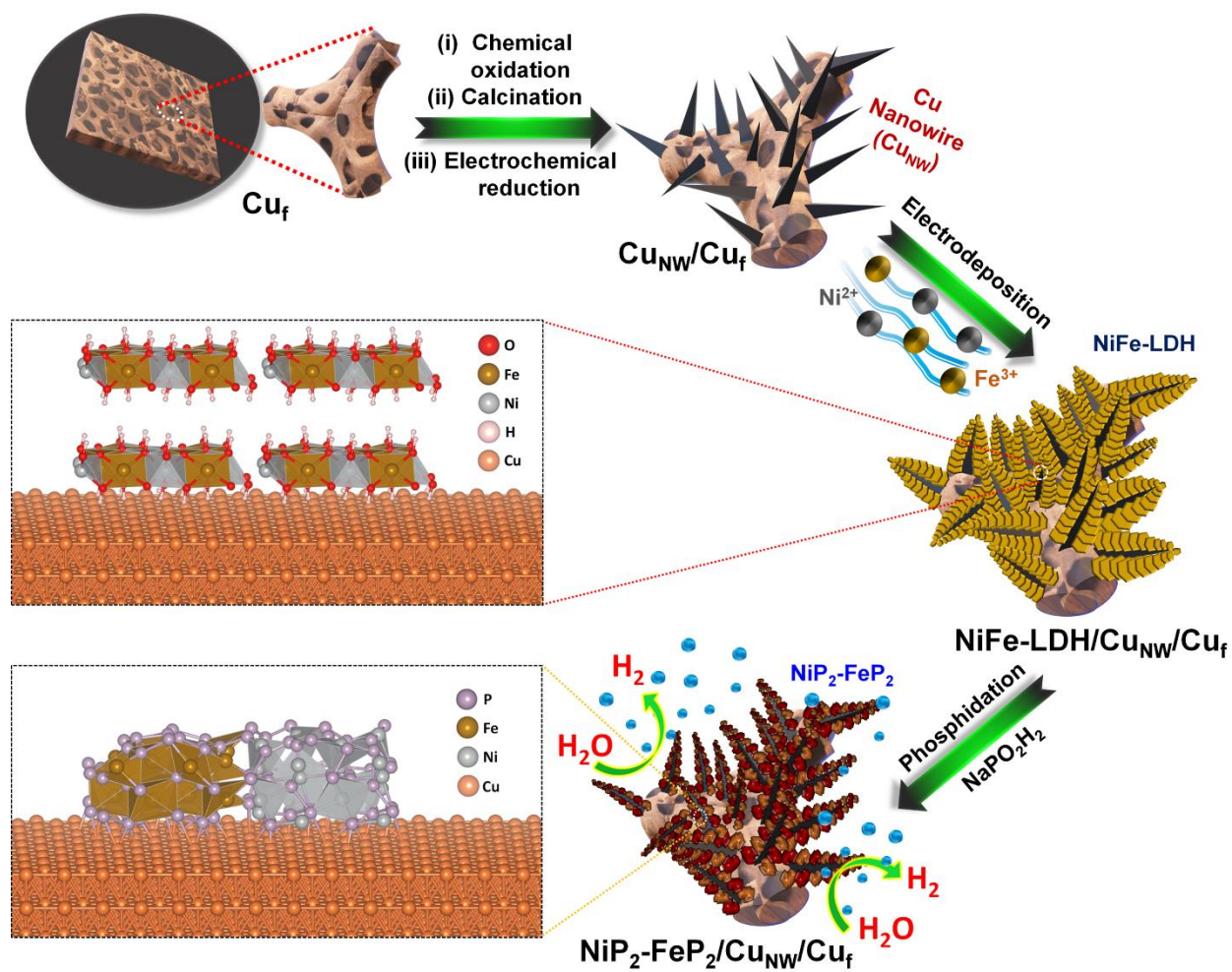


Fig. 1 | Schematic illustration of the synthesis process of $\text{NiP}_2\text{-FeP}_2/\text{Cu}_{\text{NW}}/\text{Cu}_f$.

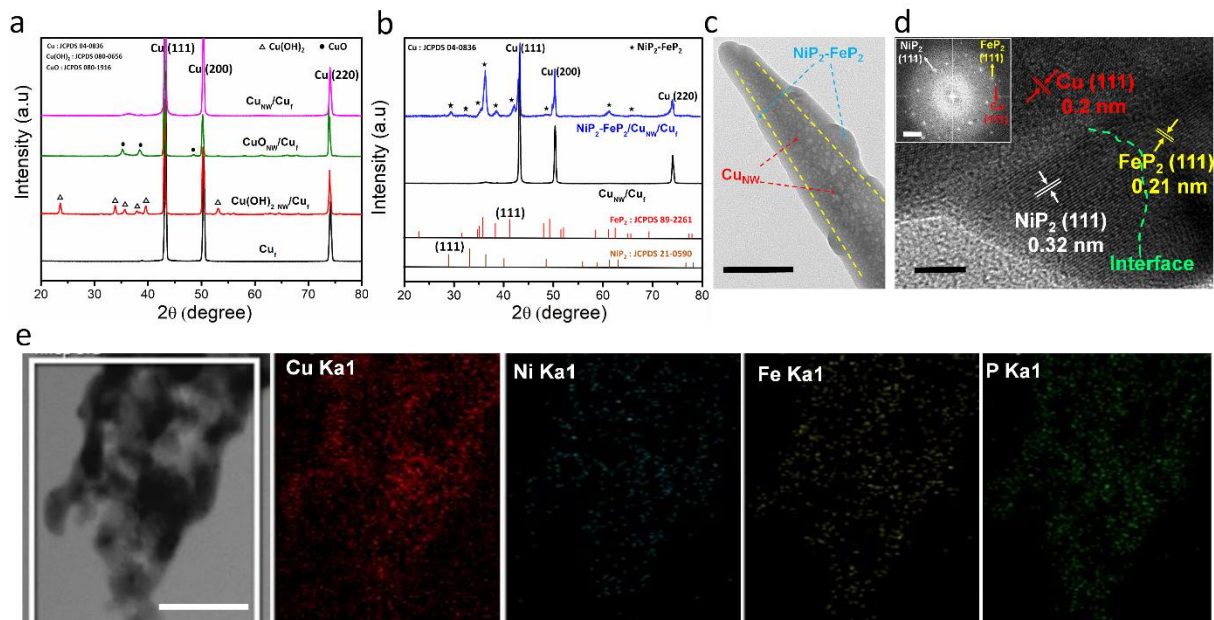


Fig. 2 | XRD patterns, TEM images, and HAADF-STEM mapping. **a,b**, XRD pattern of electrodes formed during the synthetic steps **(a)** and $\text{NiP}_2\text{-FeP}_2/\text{Cu}_{\text{NW}}/\text{Cu}_{\text{f}}$ electrode **(b)**. **c,d**, TEM (scale bar = 100 nm) **(c)** and high-resolution TEM images **(d)** (scale bar = 5 nm) of $\text{NiP}_2\text{-FeP}_2/\text{Cu}_{\text{NW}}/\text{Cu}_{\text{f}}$. The inset shows in **d** the corresponding SAED pattern of the electrode (scale bar 2 1/nm). **e** HAADF-STEM mapping of the $\text{NiP}_2\text{-FeP}_2/\text{Cu}_{\text{NW}}/\text{Cu}_{\text{f}}$ electrode (scale bar = 100 nm).

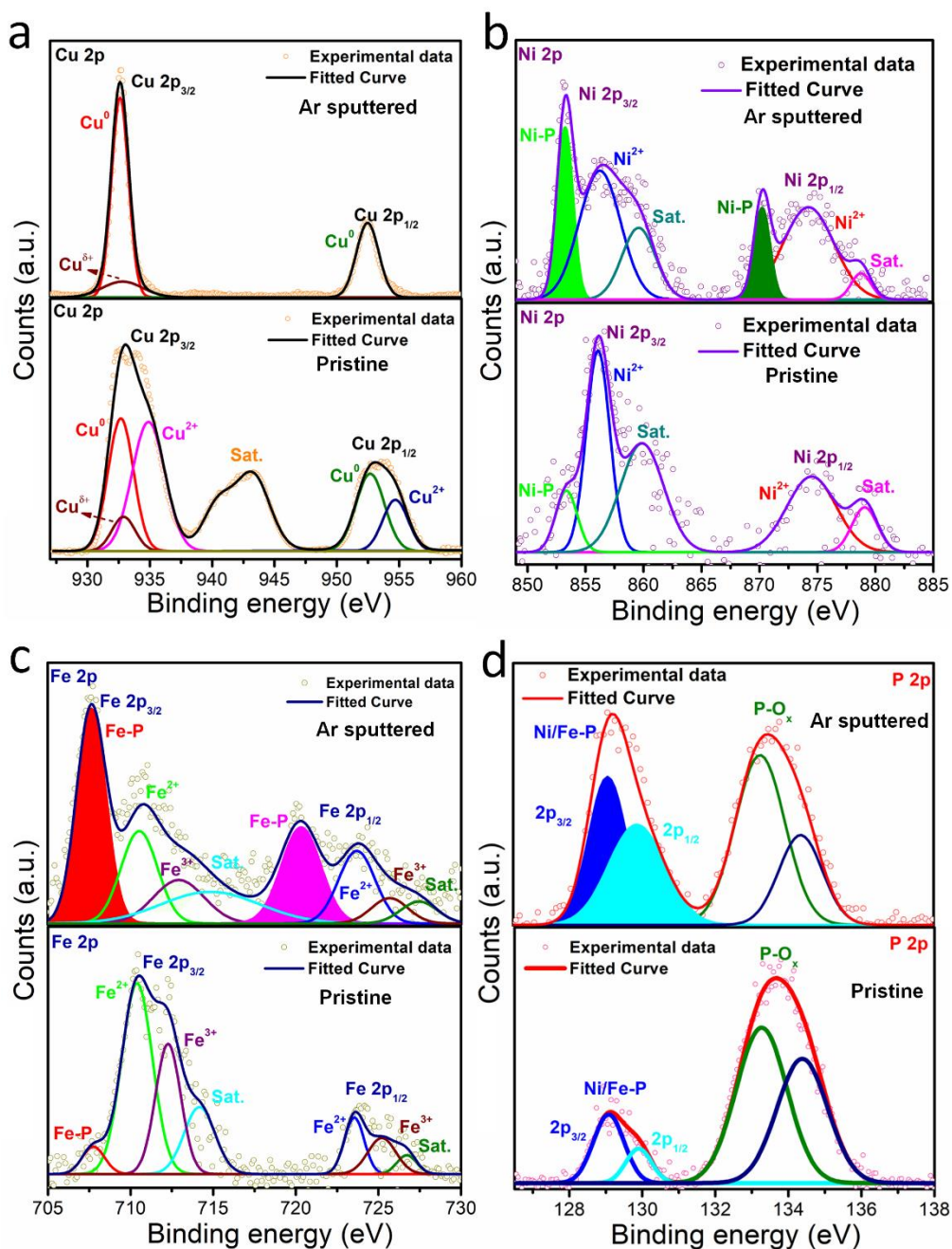


Fig. 3 | XPS spectra of the NiP₂-FeP₂/Cu_{NW}/Cu_f electrodes before and after Ar sputter. a-d, Fitted deconvoluted spectra of Cu 2p (a), Ni 2p (b), Fe 2p (c), and P 2p (d).

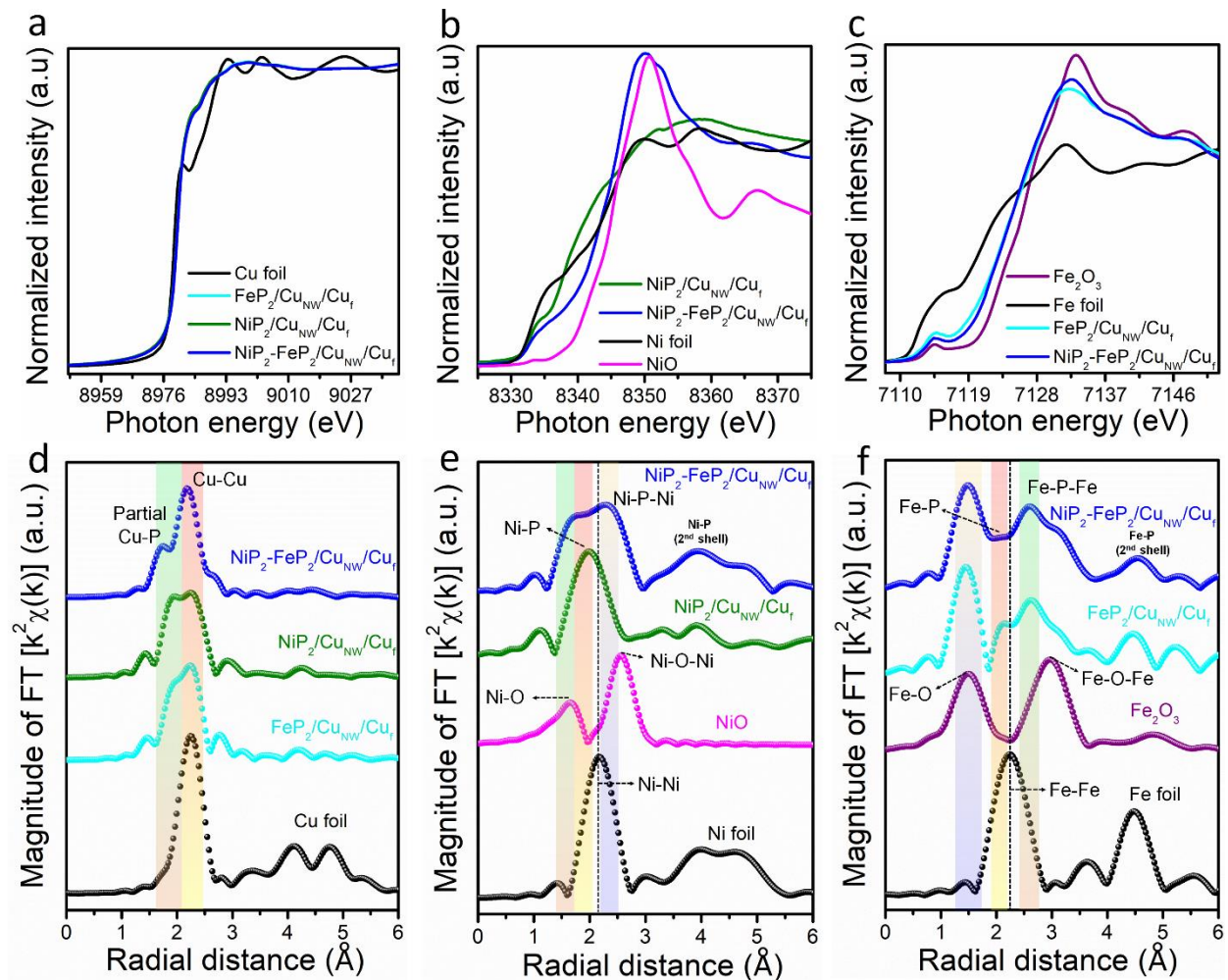


Fig. 4 | Normalized XANES and FT-EXAFS spectra collected on different samples (NiP₂-FeP₂/Cu_{NW}/Cu_F, NiP₂/Cu_{NW}/Cu_F and FeP₂/Cu_{NW}/Cu_F electrodes). a-c, Comparison of Cu K-edge (a), Ni K-edge (b) and Fe K-edge (c) XANES spectra. d-f, Comparison of Cu (d), Ni (e) and Fe (f) FT-EXAFS data in R-space collected on pristine NiP₂-FeP₂/Cu_{NW}/Cu_F electrode with other control samples.

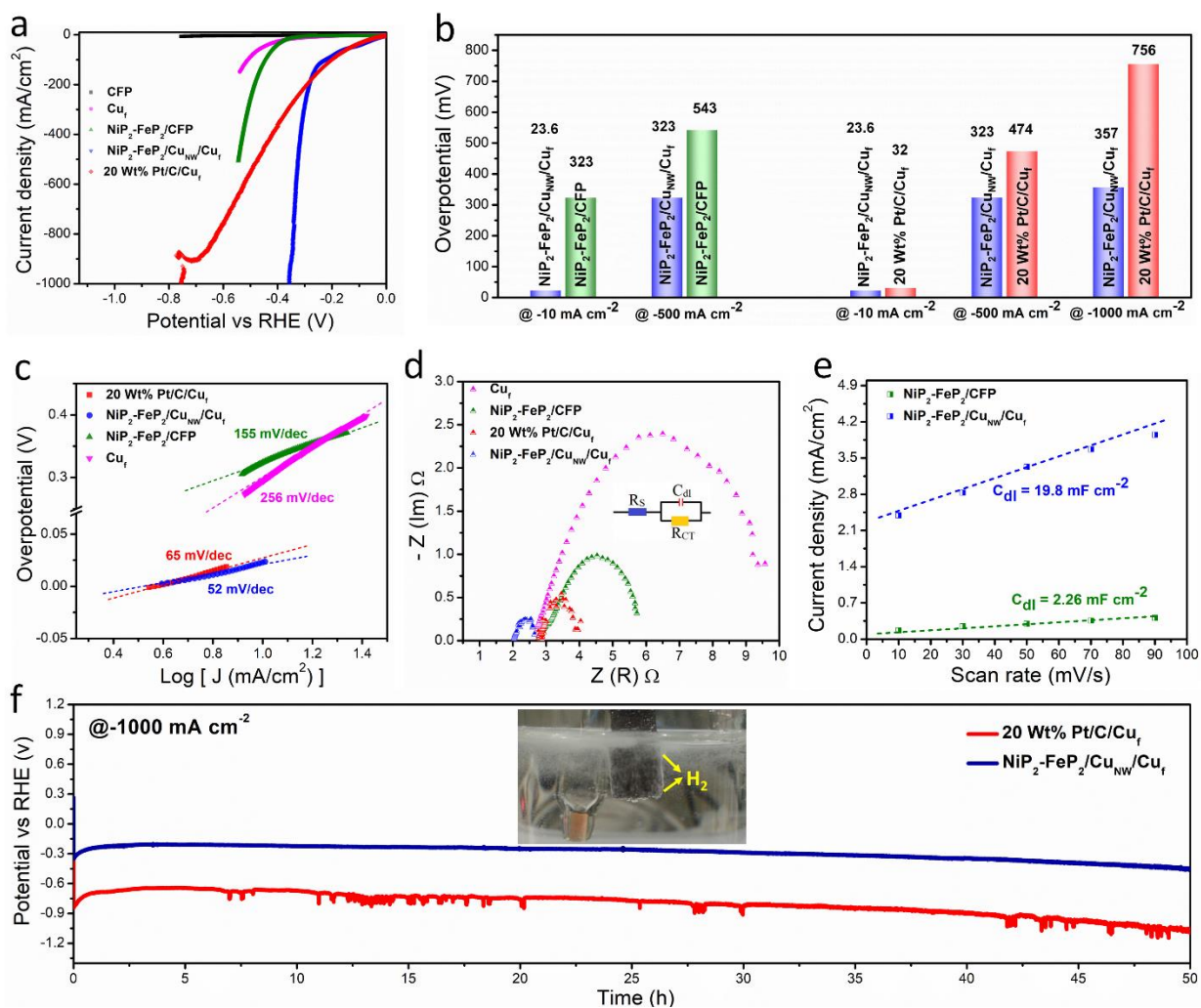


Fig. 5 | Electrochemical performance towards HER in basic media. a-f, HER polarization curves (iR-corrected) with a scan rate of 10 mV s^{-1} in 1 M KOH (**a**), the overpotentials required to reach -10 , -500 , and $-1,000 \text{ mA cm}^{-2}$ (**b**), corresponding Tafel plots (**c**), Nyquist plots taken at 374 mV overpotential (iR-uncorrected) (**d**), current density (recorded at a fixed potential) as a function of the scan rate for the extraction of the double-layer capacitance (C_{dl}) (**e**), and chronopotentiometric stability test for $\text{NiP}_2\text{-FeP}_2/\text{Cu}_{\text{NW}}/\text{Cu}_f$ and $20 \text{ wt\% Pt/C/Cu}_f$ at a high current density of $-1,000 \text{ mA cm}^{-2}$ (**f**) (inset: H_2 bubbles released during the stability test).

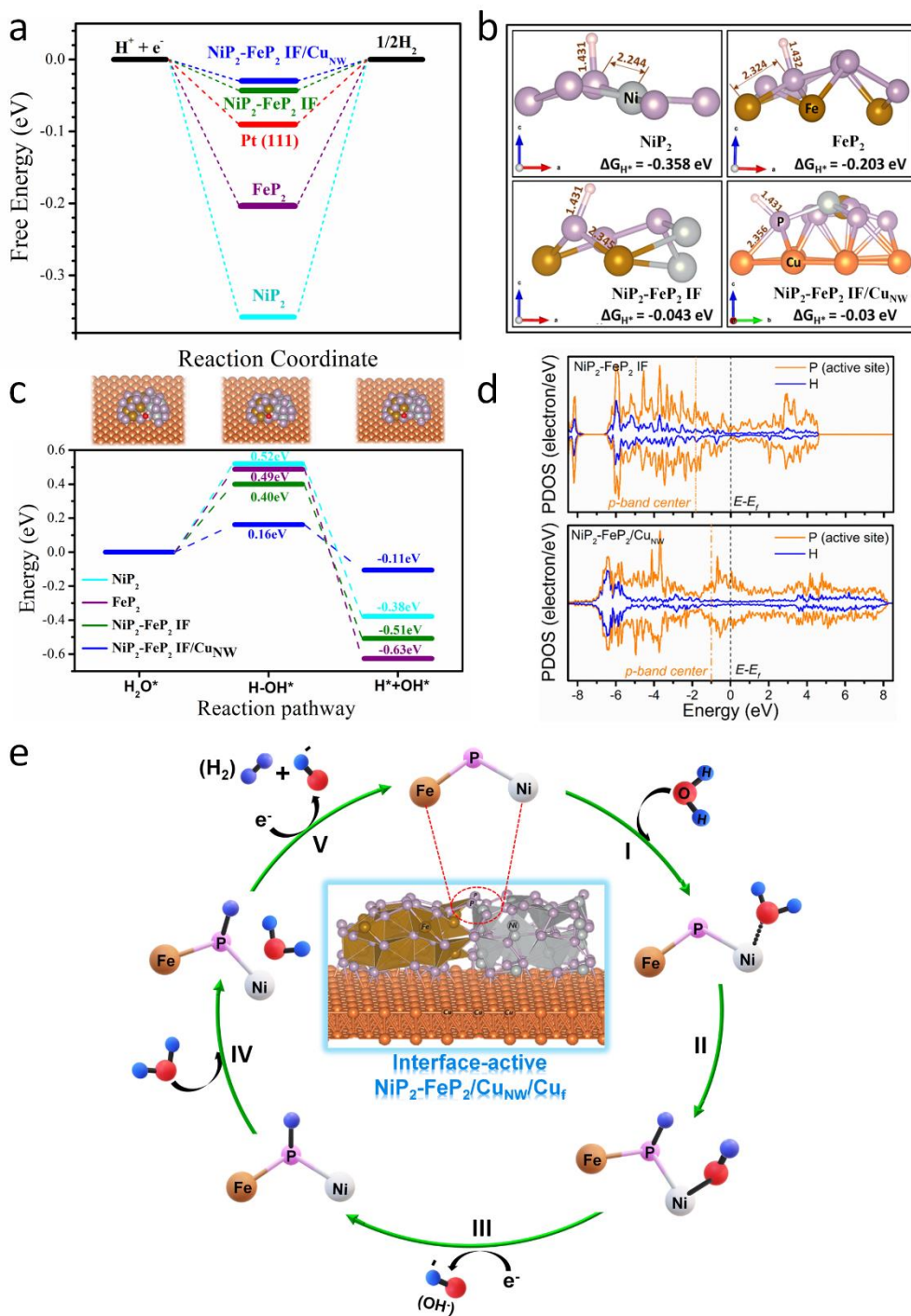


Fig. 6 | DFT calculations. **a-e**, Free energy diagrams for H adsorption in comparison to benchmark Pt catalyst (**a**), the local structures with H* atoms on FeP_2 , NiP_2 , $NiP_2-FeP_2 IF$, and $NiP_2-FeP_2 IF/Cu_{NW}$ (**b**), water dissociation potential (**c**), the P 3p partial density of states for $NiP_2-FeP_2 IF$ with/without Cu_{NW} (**d**) and optimized mechanistic pathway for alkaline HER on interface active $NiP_2-FeP_2/Cu_{NW}/Cu_f$ (**e**).

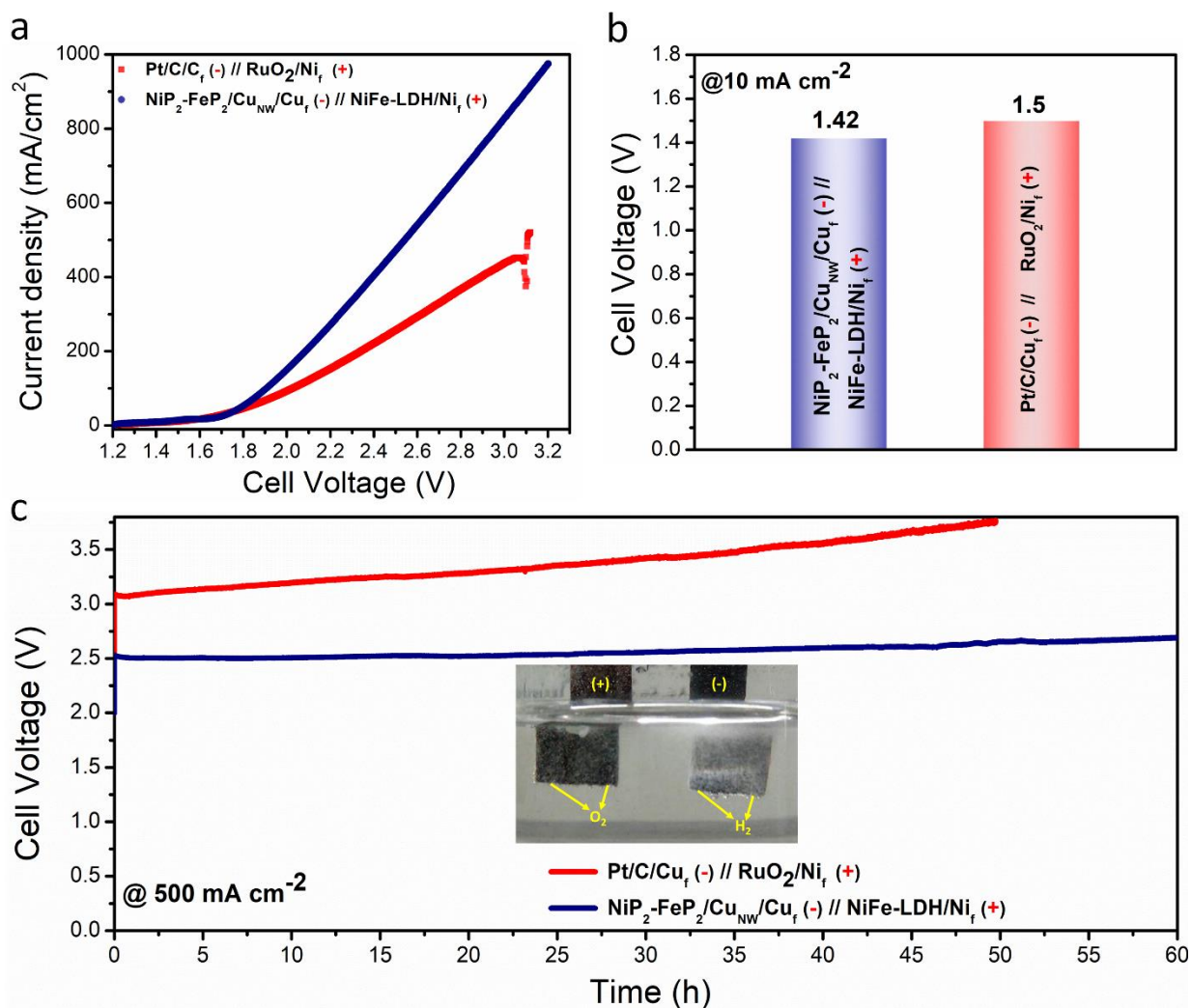


Fig. 7 | Overall electrochemical water splitting performance in two-electrode configurations. **a,b**, LSV polarization curve of the two-electrode setup for overall water splitting in 1 M KOH (iR uncorrected) (**a**) and the required cell voltage to achieve 10 mA cm^{-2} (**b**). **c**, Chronopotentiometry of water electrolysis at a current density of 500 mA cm^{-2} for the $\text{NiP}_2\text{-FeP}_2/\text{Cu}_{\text{NW}}/\text{Cu}_f$ (-) // $\text{NiFe-LDH}/\text{Ni}_f$ (+) and $\text{Pt}/\text{C}/\text{Cu}_f$ (-) // RuO_2/Ni_f (+) electrolyzer (inset: oxygen and hydrogen gas bubbles released during the stability test).

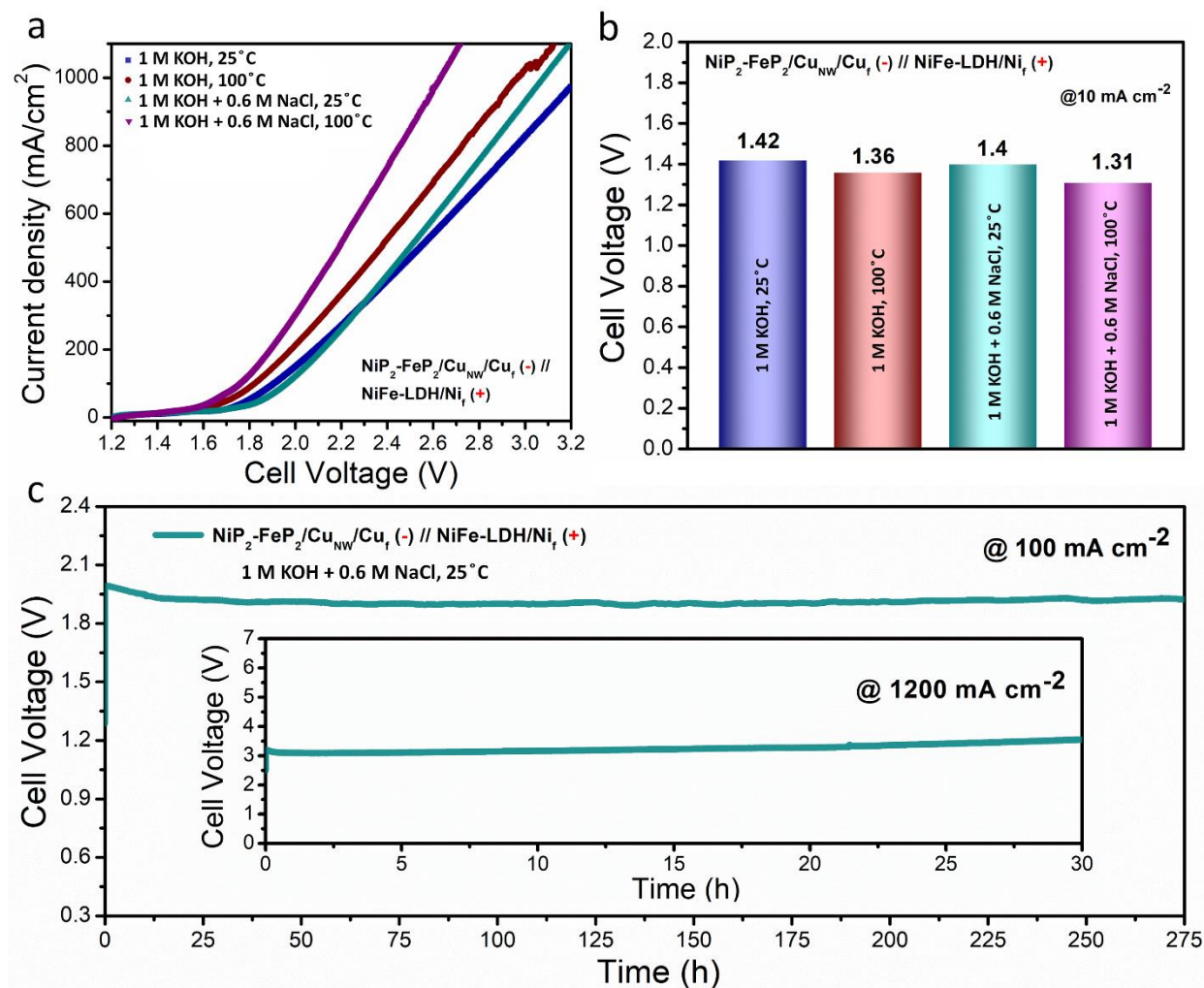


Fig. 8 | Seawater electrolysis at an elevated temperature. a,b, LSV polarization curve of the two-electrode setup for overall water-splitting in 1M KOH with 0.6 M NaCl at different temperatures (artificial seawater) (iR uncorrected) **(a)** and the required cell voltage to achieve 10 mA cm^{-2} for the $\text{NiP}_2\text{-FeP}_2/\text{Cu}_{\text{NW}}/\text{Cu}_f (-) // \text{NiFe-LDH}/\text{Ni}_f (+)$ electrolyzer **(b)**. **c**, Chronopotentiometry of water electrolysis at a current density of 100 mA cm^{-2} for the $\text{NiP}_2\text{-FeP}_2/\text{Cu}_{\text{NW}}/\text{Cu}_f (-) // \text{NiFe-LDH}/\text{Ni}_f (+)$ electrolyzer in 1 M KOH with 0.6 M NaCl at 25° C-seawater (inset: stability test of the same electrolyzer at an extremely high current density of 1,200 mA cm^{-2}).

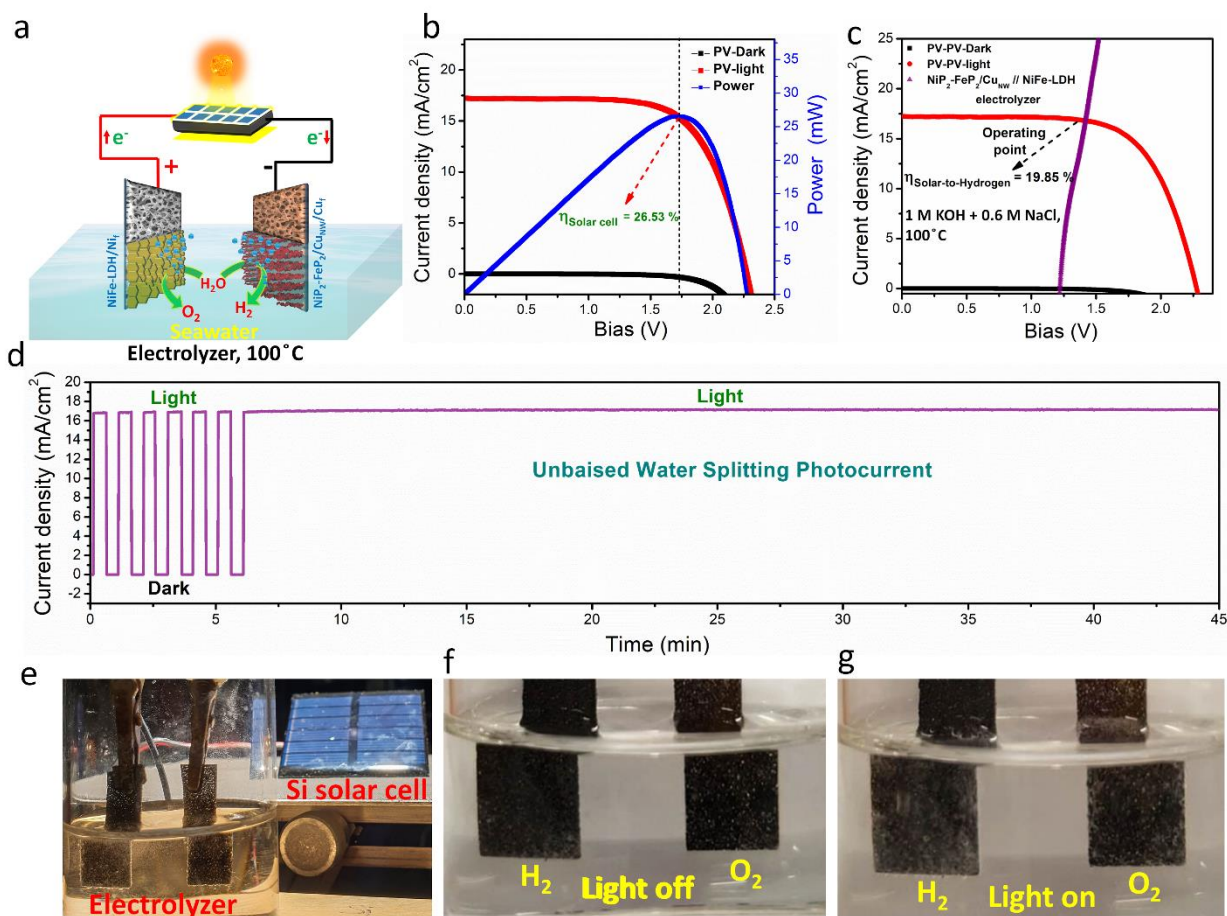


Fig. 9 | Seawater photolysis at elevated temperatures. **a**, Schematic illustration of the solar energy-driven overall seawater splitting device at a high temperature with a Si solar cell. **b**, J–V and P–V curves of the Si solar cell in the dark and under illumination. **c**, J–V curve of the Si solar cells in the dark and under illumination, and the NiP₂-FeP₂/Cu_{NW}/Cu_f (-) // NiFe-LDH/Ni_f (+) electrolyzer at a high temperature in seawater in two-electrode configurations. **d**, Current density–time curve of the integrated water splitting device without an external bias under chopped simulated AM 1.5G 100 mW cm⁻² illumination. **e–g**, Optical images of the integrated device (**e**) and the electrode surface under light off (**f**) and on conditions (**g**).

Table of Contents (TOC)

